IBI-CCS: a regional high-resolution model to evaluate western Europe sea level changes

Alisée A. Chaigneau[1,2], Guillaume Reffray[2], Aurore Voldoire[1], Angélique Melet[2]

[1]CNRM UMR 3589, Météo-France/CNRS, Toulouse, France
[2]Mercator Ocean International, Ramonville St Agne, France

Correspondence to: Alisée A. Chaigneau (achaigneau@mercator-ocean.fr)

Abstract. Projections of coastal sea level (SL) changes are of great interest for coastal risk assessment and decision-making. SL projections are typically produced using global climate models (GCMs) which cannot fully resolve SL changes at the coast due to their coarse resolution and lack of representation of some relevant processes. To overcome these limitations and refine projections at regional scales, GCMs can be dynamically downscaled through the implementation of a high-resolution regional climate model (RCM). In this study, we developed the IBI-CCS regional ocean model based on a 1/12 ° north-eastern Atlantic NEMO ocean model configuration to dynamically downscale CNRM-CM6-1-HR, a GCM with a ¼ ° resolution ocean model component developed for the Coupled Model Intercomparison Project 6th Phase (CMIP6) by the Centre National de Recherches Météorologiques (CNRM). For a more complete representation of processes driving coastal SL changes, tides and atmospheric surface pressure forcing are explicitly resolved in IBI-CCS in addition to the ocean general circulation. To limit the propagation of climate drifts and biases from the GCM into the regional simulations, several corrections are applied to the GCM fields used to force the RCM. The regional simulations are performed over the 1950 to 2100 period for two climate change scenarios (SSP1-2.6 and SSP5-8.5). To validate the dynamical downscaling method, the RCM and GCM simulations are compared to reanalyses and observations over the 1993-2014 period for a selection of ocean variables including SL. Results indicate that large-scale performances of IBI-CCS are better than those of the GCM thanks to the corrections applied to the RCM. Extreme SLs are also satisfactorily represented in the IBI-CCS historical simulation. Comparison of the RCM and GCM 21st century projections show a limited impact of increased resolution (1/4° to 1/12°) on SL changes. Overall, bias corrections have a moderate impact on projected coastal SL changes projections, except in the Mediterranean Sea where GCM biases were substantial.

1 Introduction

Sea level (SL) changes are a major threat for coastal and low-lying regions. Higher SLs can lead to coastal flooding, erosion, salinization of surface waters and groundwater, degradation of coastal ecosystems such as mangroves and coral reefs, and permanent submergence of land and human settlements (Oppenheimer et al., 2019). Risks associated to sea level rise (SLR) are even more important because coastal regions are subject to an increasing anthropogenic pressure with 10 % of the world's population living in low elevation coastal zones (McGranahan et al., 2007). In Europe, the coastal population represents 50 million people (Neumann et al., 2015). Without adaptation measures, the annual number of European people exposed to coastal flooding could reach 1.5 to 3.6 million by the end of the century and the associated expected annual damage could reach 90 to 960 billion euros (Vousdoukas et al., 2018a). Projections of coastal SL changes are thus of great interest for coastal risk assessment and decision-making processes.

Variations of the SL at the coast result from the superposition of global mean sea level (GMSL), regional SL and local SL changes (e.g. Fox-Kemper et al., 2021; Oppenheimer et al., 2019; Woodworth et al., 2019). Global mean sea level rise (GMSLR) is driven by the ocean thermal expansion and the transfer of water mass from the cryosphere and land to the ocean

(Church et al., 2013; Slangen et al., 2017). At regional scales, SL changes spatial variations are mainly due to ocean circulations and the associated ocean heat, salt and mass redistribution within the ocean (Forget and Ponte, 2015; Meyssignac et al., 2017a). At coastal scales, variations of SL are mostly related to tides, waves and atmospheric surges (e.g. Melet et al., 2018; Woodworth et al., 2019). Atmospheric surges are defined here as SL changes due to surface atmospheric

45 pressure and to local SLR caused by the wind called wind setup. At the coast, departures from the GMSL can therefore be substantial (Kopp et al., 2014; Meyssignac et al., 2017b; Melet et al., 2020). Local relative SL change information is thus required by policy makers.

SL projections are typically based on global climate models (GCMs) (Oppenheimer et al., 2019; Church et al., 2013; Slangen

50 et al., 2014). However, the typical CMIP5/6 (Coupled Model Intercomparison Project 5/6th Phase) model resolutions (mostly 1 °, ¼ °) do not allow to resolve fine scale processes. These coarse resolutions limit the realism of the representation of coastal dynamical processes influencing SL changes at the coast (Woodworth et al., 2019), potentially leading to substantial biases. For example, van Westen et al., 2020 demonstrated for the Caribbean Sea that adequate regional projections of SL changes can only be obtained with ocean models that capture mesoscale processes. In addition, GCMs do

55 not explicitly resolve key processes driving SL changes at the coast (e.g. waves, tides).

Dynamical downscaling (DD) methods can be used to refine GCM projections at regional scales by increasing the model spatial resolution and by explicitly including more processes. Such methods rely on the implementation of a high-resolution regional climate model (RCM) driven by GCM outputs. Several studies have investigated future changes in ocean

60 temperature, salinity, circulation and SL thanks to DD in various regions (e.g. Mathis et al., 2013; Adloff et al., 2018, 2015; Shin and Alexander, 2020; Gomis et al., 2016; Macias et al., 2018). Some of them have focused on SL projections particularly (Hermans et al., 2020; Liu et al., 2016; Zhang et al., 2017; Jin et al., 2021). Hermans et al., 2020 show the influence of DD for dynamic sea level (DSL) projections over the twenty-first century on the north-western European shelf using two GCMs. For the scenario with the highest radiative forcing by the end of the century (RCP8.5), they found that the

65 downscaled DSL changes can be up to 15.5 cm smaller than in the GCM simulations. These differences are found in some coastal areas owing to unresolved processes in the GCM. For the north Pacific, Liu et al., 2016 have performed a DD with 3 different CMIP5 GCMs. They showed that the downscaled SL changes can differ up to 10 cm from the GCM changes on coastal areas. Zhang et al., 2017 demonstrated the benefits of DD for Australian SL projections with a better representation of ocean gyre circulation and currents. Jin et al., 2021 have used the DD method with 8 different GCMs to provide a

70 modeling protocol to produce climate projections at low computational cost. Their results reveal greater spatial details in the downscaled simulations with differences up to 15 cm compared to the GCM simulations.

GCMs exhibit various biases when compared to observations (e.g. Flato et al., 2013). Because GCMs are used to force RCMs, these biases could propagate into regional simulations and be an important source of regional biases and uncertainties

75 for the projections (Takayabu et al., 2016; Dosio, 2016). The DD method can be used to overcome this problem by applying corrections to the GCM outputs before using them as forcing when performing a DD (e.g. Shin and Alexander, 2020). A simple method for bias correction is to simply shift the GCM data by its mean bias of a reference period. This method is used with a seasonal bias correction on the sea surface temperature (SST) in Adloff et al., 2015 and seasonal bias correction on the sea surface height (SSH) in Adloff et al., 2018. The delta correction or anomaly forcing is another commonly used

80 method: the GCM projected changes are added to a reference past state from a reanalysis data or a climatology (Jin et al., 2021; Adloff et al., 2015). Other methods exist such as rescaling the data with a factor or adjusting different ranges of a distribution individually like in Macias et al., 2018 on atmospheric variables to run an ocean model. Emergent constraints

methods also exist to overcome model biases and reduce the uncertainties of the projections (Chen et al., 2020; Grinsted and Christensen, 2021; Forster et al., 2021).

85

The aim of the present study is to provide projections of SL changes in the north-eastern Atlantic region bordering western Europe, focusing on methodological aspects. More specifically, we assess the influence on modeled regional SL changes of: (1) the DD i.e. the increased model resolution and a more complete representation of coastal processes driving SL changes and (2) bias corrections of GCM-forcing fields. To these aims, a regional DD of simulations from a high-resolution CMIP6

90 GCM is performed. The high-resolution regional ocean model includes coastal processes such as tides and surface atmospheric pressure forcing in addition to the ocean general circulation (DSL). Thanks to these included processes and high frequency outputs of the RCM, the regional simulations will be used in a future study to investigate the projections of extreme SLs over the same region. In the present study, which investigates the added value of the DD and bias corrections, the regional simulations are compared to original GCM simulations over the historical period and the 21st century using two

95 climate change scenarios.

The paper is organized as follows: the downscaling setup, correction methods, simulations performed and description of SL in the simulations are presented in Sect. 2. The DD method is evaluated in Sect. 3.1. Sect. 3.2 shows the RCM and GCM projections over the 21st century for the SSP5-8.5 and SSP1-2.6 climate change scenarios with a focus on SL changes. In

100 Sect. 3, the added value of the DD and the impact of the bias corrections applied are assessed for the simulation of past and future ocean conditions with a SL focus. The discussion and conclusions of the study are presented in Sect. 4.

2 Methods

The regional ocean climate model (RCM), called IBI-CCS (Iberian-Biscay-Ireland Climate Change Scenarios) is developed and presented in Sect. 2.1.2. In this study, IBI-CCS is forced by the CNRM-CM6-1-HR CMIP6 climate model (Sect. 2.1.1)

105 using ocean and atmospheric outputs at the lateral and air-sea boundaries of the regional IBI domain (Sect. 2.2.1). Several corrections are applied to the GCM forcings to limit the propagation of climate drifts and biases into the regional simulations (Sect. 2.2.2).

2.1 Model and configuration

The ocean component of the global climate model CNRM-CM6-1-HR and the ocean regional model IBI-CCS are based on

110 the 3.6 version of NEMO and rely on the Boussinesq approximation and a hydrostatic equilibrium (Madec et al., 2017). Both vertical grids contain 75 z-levels with a resolution decreasing from about 1 meter in the upper 10 meters to more than 400 meters in the deep ocean. A partial step representation (Barnier et al., 2006) is implemented for the bottom ocean cell to better represent the bathymetry and the model benefits from variable volume-free sea surface.

2.1.1 Global climate model, CNRM-CM6-1-HR

115 The global climate model used to force the regional ocean model is the CNRM-CM6-1-HR ocean-atmosphere coupled model, developed jointly by the Centre National de Recherches Météorologiques (CNRM) and Centre Européen de Recherche et de Formation Avancée en Calcul Scientifique (CERFACS). CNRM-CM6-1-HR contributes to CMIP6. The ocean component grid of this GCM has a 0.25 ° horizontal nominal resolution (≈ 12-25 km at 25-65° N) with refinements in the equatorial band. CNRM-CM6-1-HR is a high-resolution model compared to CMIP6 typical resolution of 1 °. CNRM-

120 CM6-1-HR is the high-resolution version of the 1 ° resolution CNRM-CM6-1, which is described in Voldoire et al., 2019; Roehrig et al., 2020. Some comparisons of CNRM-CM6-1-HR and CNRM-CM6-1 are included in Sect. 3 to assess the

impact of the increased resolution between the two GCMs. A polynomial representation of the equation of state (TEOS-10, Roquet et al., 2015) is used but the temperature and salinity outputs are converted into the in-situ temperature and practical salinity needed by the RCM. The vertical mixing of tracers and momentum uses the turbulent kinetic energy scheme (Gaspar

125   et al., 1990; Blanke and Delecluse, 1993) and the internal wave-induced mixing parameterization of de Lavergne et al., 2020. Tracers advection is computed with the centered second order formulation combined with the limiter of Zalesak, 1979. The solar penetration is parameterized according to a four-bands scheme. The NEMO ocean model and a sea-ice scheme GELATO are coupled to a land-atmosphere model using the OASIS-MCT coupler. The atmospheric component is the global atmospheric model ARPEGE-Climat 6.3 with a horizontal resolution of 0.5 ° (≈ 24-50 km at 25-65° N) at the Equator.

130   Several GCM simulations are used to prepare the forcings required to force the RCM: a historical run (1850-2014) forced by observed greenhouse gas concentrations, a preindustrial control run forced by fixed preindustrial conditions representative of the 1850s over 300 years and scenarios (2015-2100) based on alternative trajectories for future emissions. In this paper, we focus on two contrasting scenarios included in Tier1 of ScenarioMIP: SSP5-8.5 and SSP1-2.6 with respectively a very high and low radiative forcing by the end of the century (O'Neill et al., 2016). The SSP5-8.5 scenario relies on a fossil-fuel based

135   world development leading to an Earth radiative imbalance of 8.5 W m^{-2} in 2100. This scenario approximatively corresponds to the CMIP5 RCP8.5 scenario. The SSP1-2.6 scenario has a 50 % chance to follow the Paris agreement of a limited warming below 2 °C by the end of the century and corresponds to the CMIP5 RCP2.6 scenario.

2.1.2 Regional ocean model IBI-CCS
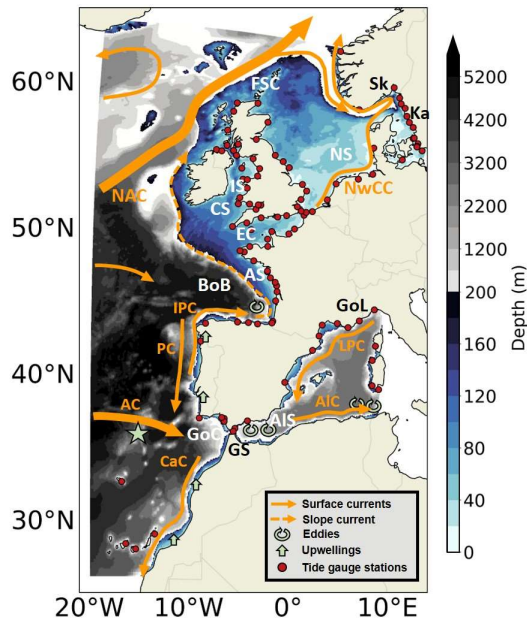
140   **Figure 1: Bathymetry (m) and schematic description of main oceanographic features in the IBI domain. The main surface dynamical features shown are: the North Atlantic Current (NAC), the Azores Current (AC), the Canary Current (CaC), the Portugal Current (PC), the Iberian Poleward Current (IPC), the Norwegian Coastal Current (NwCC), the Liguro Provençal Current (LPC), the Algerian Current (AlC). Some geographical features are mentioned: the Bay of Biscay (BoB), the Armorican Shelf (AS), the English Channel (EC), the Irish Sea (IS), the Celtic Sea (CS), the North Sea (NS), the Faroe - Shetland Channel**
145   **(FSC), the Kattegat (Ka), the Skagerrak (Sk), the Gulf of Cadiz (GoC), the Alboran Sea (AlS), the Gulf of Lion (GoL) and the Gibraltar Strait (GS). The star indicates the zone where a TS diagram is performed in Sect. 3.1.3. The red dots represent the tide gauge stations of the zone used in Sect. 3.1.6. Note that the color scale for the bathymetry is not linear.**

The domain covered by the regional ocean model is the Iberian-Biscay-Ireland (IBI) zone, extending from 25° N to 65° N
150 and 21° W to 14° E. This region includes the north-eastern Atlantic Ocean, the North Sea and the western Mediterranean Sea
(Fig. 1). The IBI zone is covered in the framework of the Copernicus Marine Service (CMEMS) with a 1/36 ° real-time
system and a 1/12 ° reanalysis IBIRYS (https://marine.copernicus.eu/about/producers/ibi-mfc). The ocean reanalysis
IBIRYS is described in CMEMS-IBI-PUM-005-002.pdf (copernicus.eu) and validated in CMEMS-IBI-QUID-005-002.pdf
(copernicus.eu). The configuration of this reanalysis is based on a curvilinear grid at a 1/12 ° horizontal resolution (≈ 4-8.5
155 km at 25-65° N) and is used for the IBI-CCS simulations. A variety of physical oceanographic processes are found in this
region (Sotillo et al., 2015; Maraldi et al., 2013). First, the zone contains strong variations of bathymetry with a wide
continental shelf in the northern part of the domain (North Sea, English Channel) and a tight continental shelf in the southern
part (Spain, Portugal, Morocco, Mediterranean Sea) (Fig. 1). The north-western deeper part of the IBI region is mainly
driven by the North Atlantic Current (NAC). Along the continental slope, a poleward slope current flows from the
160 Portuguese coasts to the north of Ireland with slope oceanic eddies along the northern Iberian coast. On the continental
shelves, large energetic tides are particularly found in the English Channel, Celtic and Irish Seas. In the southern part of the
domain, two main physical features are found: strong summer upwellings along the Portuguese and Moroccan coasts and
Gibraltar Strait. At Gibraltar Strait, exchanges between the Atlantic Ocean and Mediterranean Sea occur and drive mesoscale
eddies in the Alboran Sea (Fig. 1).

165 The main added value of this configuration in comparison to the GCM (Sect. 2.1.1) is the inclusion of processes driving SL
changes in the coastal ocean such as tides and atmospheric pressure forcing in addition to the ocean general circulation
(DSL). Tides are included in the model by calculating the astronomical tidal potential and the tidal harmonic forcing as the
sum of 11 components: diurnal components (K1, O1, P1 and Q1), semi-diurnal constituents (M2, S2, N2 and K2), long-
period-tides (Mf and Mm) and a nonlinear component M4. In addition to these high frequency processes added in the RCM,
170 some physical parameterizations also differ from those of the GCM. Seawater thermodynamics uses a polynomial
approximation of EOS-80 (Fofonoff and Millard Jr, 1983). Vertical mixing is parameterized according to a k-ε model
implemented in the generic form proposed by (Umlauf and Burchard, 2003; Reffray et al., 2015). Although tides are
explicitly treated, the mixing induced by internal tides is not completely resolved in the RCM and the parameterization of de
Lavergne et al., 2020 is also activated in the RCM (as in the GCM). Tracers advection is computed with the QUICKEST
175 scheme developed by Leonard, 1979 combined with the limiter of Zalesak, 1979. The solar penetration parameterization is
based on a five-bands exponential scheme. Finally, air-sea turbulent fluxes are calculated in the model using ECMWF-IFS
bulk formulations (ECMWF, 2014; Brodeau et al., 2017).

2.2 Regionally downscaled simulations

The regionally downscaled simulations are performed over the 1950-2100 period. 1950-1970 is considered as the spin-up
180 period after which surface and intermediate waters have reached a quasi-equilibrium (not shown here). The historical
regional simulation therefore starts in 1970 and ends in 2014. Climate change simulations using scenarios described in Sect.
2.1.1 are run from 2015 to 2100.

The near surface atmospheric state variables from the GCM used to force the regional ocean model are the three-hourly 2m-
185 air temperature (t2m), 2m-specific humidity (q2m), 10m-wind, short and long wave radiations, precipitation and six-hourly
atmospheric pressure at SL. The open boundary conditions (OBCs) are prescribed at the lateral boundaries of the regional
domain each month using the GCM 3D ocean temperature, salinity, currents and 2D sea surface height (SSH). A buffer zone
of 10 grid points (except at the eastern boundaries where 5 grid points are used) relaxes the internal regional solution to the
prescribed boundary values. For the SSH forcing, the GCM SSH is not directly prescribed but enters in a Flather-type

190   algorithm (Flather and Davies, 1976). The RCM is initialized using temperature, salinity, currents and SSH variables. Monthly runoff from GCM are also prescribed to the RCM.

Global climate models are typically subject to drift (i.e long-term change independent of internal variability or external forcings, especially in the deep ocean, Gupta et al., 2013) and to substantial biases (Flato et al., 2013, Fasullo, 2020). To

195   prevent the regional simulations from inheriting the drift and biases of the GCM, several corrections have been applied to the GCM outputs before prescribing them to the RCM. Two different simulations are performed to assess the impact of these corrections (Table 1). The first one is the raw simulation referred to as IBI-CCS_raw without any correction of the GCM forcings (Sect. 2.2.1). The second one is referred to as IBI-CCS_corr with corrections of the GCM forcings (Sect. 2.2.2). A third simulation called IBI-ERAi is performed as a reference simulation to validate the IBI-CCS_raw and IBI-CCS_corr in

200   Sect. 3.

	Atmospheric forcings		Open boundary conditions forcings		Initial conditions	Runoff forcings	
Simulation	Fields	Freque ncy	Fields	Freque ncy	Forcing	Fields	Freque ncy
IBI-CCS_raw (1950-2100)	CNRM-CM6-1-HR	3hours	CNRM-CM6-1-HR	1 month	CNRM-CM6-1-HR	CNRM-CM6-1-HR seen by the ocean component	1 month
IBI-CCS_corr (1950-2100)	CNRM-CM6-1-HR drift (t2m, q2m) and bias (t2m, q2m, radiative fluxes) corrected	3hours	CNRM-CM6-1-HR drift and bias corrected (T,S,SSH) + SSH setting in Mediterranean Sea	1 month	CNRM-CM6-1-HR drift and bias corrected (T,S,SSH)	TRIP (river routing model of CNRM-CM6-1-HR)	1 day
IBI-ERAi (1993-2104)	ERAinterim	3hours/ 1 day	GLORYS2V4	1 day	GLORYS2V4	daily observations, simulated data and climatology (see CMEMS-IBI-PUM-005-002.pdf (copernicus.eu))	1 day

Table 1: Regional IBI-CCS and IBI-ERAi simulations forcings and settings and their corrections when applicable.

2.2.1 IBI-CCS_raw simulation

For the IBI-CCS_raw simulation, atmospheric and OBC forcings, initial conditions and runoffs are directly taken from the

205   GCM outputs without any correction by extraction and interpolation on the 1/12° regional grid. The RCM is initialized using the GCM state of January 1950 for temperature, salinity, currents and SSH. The monthly runoff outputs are taken from the ocean component of the GCM.

2.2.2 IBI-CCS_corr simulation

Drift correction

210   Due to its high resolution and thus high computational cost, CNRM-CM6-1-HR has a particularly short spin-up time of 250 years. As a consequence, the GCM is subject to large drifts relative to coarser resolution CMIP6 class models (not shown here) with longer spin-up integrations. To avoid the GCM drift effect on regionally simulated long term trends, the drift is removed from the GCM outputs before using them to force the RCM. As shown in Irving et al., 2021, in most cases, a linear fit of the preindustrial control simulation is sufficient to evaluate the drift in CMIP6 models. For the CNRM-CM6-1-HR

215   variables concerned by drifts, a linear fit is indeed appropriate. The CNRM-CM6-1-HR model drift is estimated at each grid

point by a linear fit of the full time series of the pre-industrial control simulation. Then, the linear fit is subtracted to the corresponding historical simulation and projections at each time step and grid point. The drift is removed from the air temperature and specific humidity for atmospheric forcings, and from 3D temperature, 3D salinity and 2D SSH for ocean forcings (Table 1).

220

Bias correction

To limit the GCM bias propagation into the IBI-CCS_corr projections, a simple seasonal mean bias correction (Xu et al., 2019; Adloff et al., 2015, 2018; Macias et al., 2018) is applied to the GCM outputs before using them to initialize and to force the RCM. Bias adjustments allow a more realistic ocean mean state representation and conserve the GCM variability in

225 the regional simulations. This method relies on a stationarity hypothesis, i.e. biases do not depend on the mean state and are thus assumed to be the same in historical and scenario simulations (Krinner and Flanner, 2018).

The bias corrections applied to the IBI-CCS_corr forcings are based on the oceanic reanalysis GLORYS2V4 considered as the reference dataset here. The GLORYS2V4 reanalysis distributed by CMEMS has been largely validated in Garric et al.,

230 2017; https://cmems-resources.cls.fr/documents/QUID/CMEMS-GLO-QUID-001-025-011-017.pdf. To apply these bias corrections, monthly mean differences between the GCM and GLORYS2V4 are computed over the 1993-2014 period. Then, the mean seasonal cycle of biases is subtracted to the GCM outputs at each time step, each grid point, for the past, present and future periods. This method is applied to the ocean 3D temperature, 3D salinity and 2D SSH used at the OBCs and as initial conditions (Table 1). The velocity field quickly adjusts to these corrections. For the GCM atmospheric outputs, the

235 surface (2 m) air temperature and specific humidity as well as short and long wave radiations are seasonally bias-corrected using the ERAinterim reanalysis (Berrisford et al., 2009) as reference dataset using a similar methodology as described for the OBCs. The ERAinterim reanalysis was chosen to keep the consistency with the corrections applied on the ocean as ERAinterim was used to force the GLORYS2V4 reanalysis employed to bias-correct the ocean GCM outputs.

240 **Modification of the river forcing**

In CNRM-CM6-1-HR, the way river discharges are interpolated to the ocean model grid results in large errors in regional runoff amounts, the global water budget being conserved (Voldoire, 2020). For instance, severe overestimates are found for the Rhone river runoff, one of the major rivers in the IBI western Mediterranean domain, that causes a large freshwater bias in the GCM in this region. For the IBI-CCS_corr simulation, the river runoff forcing is thus taken directly from the daily

245 runoff simulated by the river routing component of CNRM-CM6-1-HR (TRIP, Table 1) at 0.5 ° and interpolated on the 1/12 ° grid. Therefore, in IBI-CCS_corr, the RCM does not receive the same amount of runoff as in IBI-CCS_raw and as the ocean component of the GCM.

Sea Surface Height tuning in the Mediterranean Sea

250 In the Mediterranean Sea, the excess of evaporation over precipitation and river runoff is compensated by a net inflow of fresh Atlantic waters. These waters are transformed into denser waters and leave the Mediterranean Sea as deep currents through Gibraltar Strait. Therefore, realistic exchanges through the strait are of great importance for modeling volume transport and water mass properties. The net transport through Gibraltar Strait is directly related to the difference of pressure between the Atlantic Ocean and Mediterranean Sea which is linked to the difference of SSH between the two basins (Soto-

255 Navarro et al., 2010). The bias corrections (Sect. 2.2.2) allow to obtain the ocean mean state of GLORYS2V4 and thus a more realistic representation of the water masses than in the GCM. However, GLORYS2V4 has a mean SSH bias of approximately -0.1 m in the Mediterranean Sea in comparison to the Mean Dynamic Topography observations from CNES-CLS-18 (Mulet et al., 2021). As a consequence, the bias correction applied on the SSH (Sect. 2.2.2) is not sufficient to obtain

a more accurate net transport through Gibraltar Strait. A supplementary tuning has been added to improve it in the IBI-

260   CCS_corr simulation. A SSH corrective value of +0.1 m is thus applied to the east Mediterranean boundary at each time step and boundary grid point to compensate for the GLORYS2V4 bias and to obtain a proper difference of SSH between the two basins.

2.2.3 IBI-ERAi simulation

In addition to the reference IBIRYS reanalysis provided by CMEMS (Sect. 2.1.2), another reference simulation called IBI-

265   ERAi, has been performed based on the same configuration. IBI-ERAi is a free simulation (no data assimilation) forced by GLORYS2V4 and ERAinterim, which are also the two reanalyses used to diagnose bias corrections in IBI-CCS_corr (Sect. 2.2.2). IBI-ERAi is thus considered as the best simulation to be directly compared to IBI-CCS_corr to evaluate the DD of the GCM.

2.3 SL in regional simulations

270   The regional simulations performed in this study are intended to be used in particular to investigate the projections of extreme SLs. As shown in Menéndez and Woodworth, 2010; Vousdoukas et al., 2018b, changes in extreme SLs are mainly driven by SLR. We have therefore paid particular attention to the representation of GMSLR in the RCM.

2.3.1 Transfer of water mass from the cryosphere and land to the ocean

Barystatic SLR (Gregory et al., 2019) is dominated by the mass loss of glaciers and ice sheets (Oppenheimer et al., 2019).

275   While GCM can, to some extent, represent surface mass balance processes, they cannot account yet for dynamic mass loss. In CNRM-CM6-1-HR, the glaciers and Greenland mass losses are underestimated compared to projection assessments (Table 2).

Contributions to GMSL (in m)	scenario	CNRM-CM6-1-HR (2081-2100 relative to 1986-2005)	Oppenheimer et al., 2019 (2081-2100 relative to 1986-2005)	Hock et al., 2019 (2081-2100 relative to 2000)
Antarctica	SSP5-8.5	0.09	0.10 [0.02-0.23]	
	SSP1-2.6	0.05	0.04 [0.01-0.10]	
Greenland	SSP5-8.5	0.06	0.12 [0.07-0.21]	
	SSP1-2.6	0.03	0.07 [0.04-0.10]	
Glaciers	SSP5-8.5	0.04	0.16 [0.09-0.23]	0.14
	SSP1-2.6	0.03	0.10 [0.04-0.16]	0.09
Total	SSP5-8.5	0.19	0.38	
	SSP1-2.6	0.11	0.21	

Table 2: Projected global mean changes in SL mass dominating contributions for the SSP5-8.5 and SSP1-2.6 scenarios in CNRM-
280   **CM6-1-HR, Oppenheimer et al., 2019 and Hock et al., 2019.**

To estimate SLR over the IBI region due to glaciers and ice sheets mass loss, we used the fingerprints of these contributions to scale their global mean contribution to the regional domain. To that end, we used Grinsted et al., 2015 spatial fingerprints, expressed as a percentage of the GMSL contribution for the different land-ice components. The Antarctic ice sheet, Greenland ice sheet and glaciers' contributions to GMSLR simulated in CNRM-CM6-1-HR and derived from Oppenheimer

285   et al., 2019 and Hock et al., 2019 are given in Table 2. In CNRM-CM6-1-HR, the Antarctic contribution to GMSLR is similar to that of Oppenheimer et al. 2019 and Hock et al., 2019 (although probably not for the right reason), whereas the

contributions from the Greenland ice sheet and glaciers are clearly underestimated. The regional contributions obtained after applying the spatial fingerprint are presented in Fig. 2. The global mean contribution is weighted by a factor 120% for the Antarctic, 50% for the glaciers and is close to zero for Greenland (i.e. the effects of the Greenland ice mass loss on the IBI

290   zone are considered null on average due to its distance to the ice sheet). As it turns out, the sum of all the regional land ice mass contributions estimated from the literature (grey solid line in Fig. 2) is very close to the CNRM-CM6-1-HR simulated contributions for both scenarios (grey dashed line in Fig. 2). Therefore, no corrections have ultimately been applied to the GCM concerning the mass change terms.
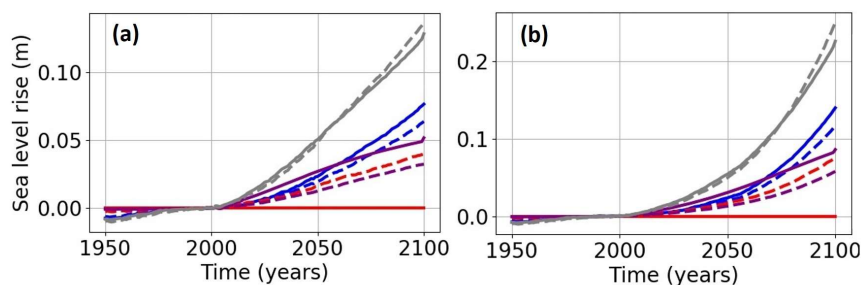
295   **Figure 2: Projected changes up to 2100 (relative to 1986-2005) of dominating barystatic SLR contributions scaled to the IBI domain using their spatial fingerprints for (a) SSP1-2.6 scenario (b) SSP5-8.5 scenario. The SL contributions evaluated here are: the Antarctic ice-sheet contribution (blue), the Greenland ice-sheet contribution (red), the glaciers contribution (purple), and their sum (grey). The dashed lines represent the initial CNRM-CM6-1-HR contributions and the solid lines the contributions based on Oppenheimer et al., 2019 for the Antarctic ice sheet and on Hock et al., 2019 for glaciers.**

300   **2.3.2 Thermal expansion**

In Boussinesq ocean models such as NEMO CNRM-CM6-1-HR or IBI-CCS, the ocean volume evolves according to the mass budget but does not change globally according to ocean density changes. The global mean thermosteric sea level rise (GMTSLR), which corresponds to a thermal expansion of the ocean, is therefore not explicitly represented in such models. As the GMTSLR is a dominant contribution to the GMSLR (Oppenheimer et al. 2019, Fox-Kemper et al. 2021), it has to be

305   evaluated a posteriori from the simulated ocean density field (Greatbatch, 1994; Griffies and Greatbatch, 2012). As the water column cannot expand, the GMTSLR cannot be prescribed directly to the RCM because any increase in volume can only result in an addition of mass. This addition of mass would be directly added at local temperature and salinity properties which would increase the pressure gradient and result in an acceleration of the circulation close to the boundaries. The GCM GMTSLR term stored in the variable "zostoga" is thus added a posteriori to the RCM modeled SL.

310   **2.3.3 Total SL in regional simulations**

Although Boussinesq models do not represent the expansion of the water column, they are able to correctly reproduce the local steric effect (Griffies and Greatbatch, 2012) related to changes in the local density of the water column through the equation of state. As non-uniform density changes create pressure gradients, the ocean circulation is dynamically adjusted (e.g. thermal wind balance) and spatial gradients of DSL are simulated (Griffies and Greatbatch, 2012). Therefore, we

315   conclude that the only missing SL term in the regional model comes from the GMTSLR. The total SL η in the IBI-CCS_raw and IBI-CCS_corr simulations is diagnosed by:

$$\eta = \text{GMTSLR} + \text{Sea Surface Height}$$
$$= \text{zostoga (GCM) (global process)} + \text{SSH (RCM) (global to coastal processes)} \quad (1)$$

320

where the SSH is the regional model sea surface height and includes global, regional and coastal processes:

- the mass variations corresponding to the freshwater balance i.e. evaporation over precipitation and river runoff (regional processes) and the transfer of water mass from the cryosphere and land to the ocean from the GCM (Sect. 2.3.1).

325
- the DSL which corresponds to the variable "zos" of the GCM but which also includes in the RCM tides, the barotropic effects due to SL pressure forcing. Main drivers of DSL are steric SL (ocean density related) and manometric SL (mass related) components (Gregory et al., 2019). The steric SL itself can be decomposed into thermosteric and halosteric components related to changes in density due to temperature and salinity changes, respectively. Following Gregory et al., 2019, the DSL is corrected by the inverse barometer (IB) effect. The latter is

330
computed based on Stammer and Hüttemann, 2008 formulation. The IB effect is included in the presented SL results unless stated otherwise.

In the following sections the term "SL" refers to the total SL η.

3 Results

3.1 Historical simulations and validation of the ocean regional climate model

335   To validate the DD method, the IBI-CCS_raw, IBI-CCS_corr and CNRM-CM6-1-HR historical simulations are compared to the reanalysis IBIRYS, the IBI-ERAi regional simulation and observational datasets over the 1993-2014 period. The comparisons are performed at different time scales for a selection of ocean variables including SL. Due to the chaotic nature of the climate system, GCMs do not follow the real-world internal variability chronology, but they should represent a climate internal variability that is statistically similar to the observed one. Consequently, only the capabilities of the model to

340   reproduce observed distributions are assessed. In this section, in addition to the validation of the IBI-CCS regional simulations, the added value of the DD (in terms of resolution and added physical processes) and of the bias corrections applied are investigated.

3.1.1 Thermosteric, Halosteric, Steric and Manometric SL
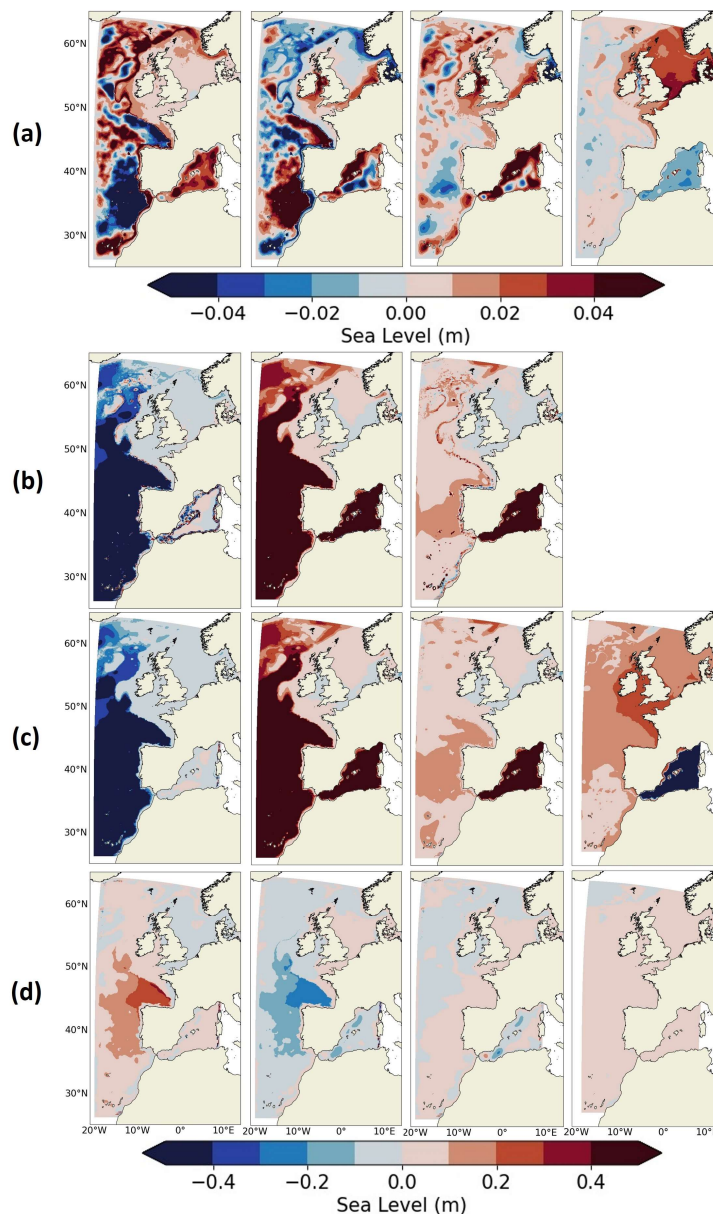
345   **Figure 3: Thermosteric (first column), halosteric (second column), steric (third column) and manometric (last column) SL bias over 1993-2014 between (a) IBI-ERAi and IBIRYS, to show biases in the IBI-ERAi simulation, and between (b) CNRM-CM6-1-HR and IBI-ERAi, (c) IBI-CCS_raw and IBI-ERAi, (d) IBI-CCS_corr and IBI-ERAi. Manometric SL biases between CNRM-CM6-1-HR and IBI-ERAi are not shown here as they mostly display the differences of bathymetry between the two models. The thermosteric, halosteric and steric components have been computed over 0-2000 m depth. Note the different colorbars in panel (a)**
350   **and in panels (b), (c), (d).**

Figure 3 compares the main components of DSL (Sect. 2.3.3) averaged over the 1993-2014 period for the different simulations. As the thermosteric and halosteric SL components are depth-integrated variables, the comparisons allow to validate respectively the heat and salt content of the model between 0 and 2000 m. Differences between the reanalysis IBIRYS and IBI-ERAi highlight the biases of IBI-ERAi and do not exceed 10 cm, even in the deep ocean (Fig. 3a). Biases

355   between CNRM-CM6-1-HR and IBI-ERAi are large (Fig. 3b). Indeed, in the Atlantic Ocean, the thermosteric SL is 40 cm too low due to a large cold bias. The GCM halosteric SL is 50 cm higher than its IBI-ERAi counterpart in the Mediterranean Sea because of a fresh bias due to the strong positive bias in the Rhone river discharge received by the GCM ocean component (Sect. 2.2.2). This fresh bias seems to spread in the Atlantic Ocean through Gibraltar Strait. In the Atlantic Ocean, the thermosteric and halosteric biases balance each other leading to small biases on the steric SL. However, it is not

360   the case in the Mediterranean Sea where the halosteric bias leads to steric biases of a larger amplitude. The large biases found in the GCM propagate into IBI-CCS_raw with the same amplitude (Fig. 3c). These biases are consistent with the cold sea surface temperature and fresh salinity biases provided in the Supplementary Materials (Fig. S1 and Fig. S2).

   In IBI-CCS_corr, runoffs are directly taken from the river routing model to avoid the regional discrepancies present in the

365   GCM and subsequently in IBI-CCS_raw simulations (Sect. 2.2.2). The change of runoff results in a considerable reduction of the halosteric bias in the Mediterranean Sea. The reduction of the biases on all the different SL components in IBI-CCS_corr (Fig. 3d) is consistent with the bias correction method used to correct the GCM forcings. Indeed, the 1993-2014 period has been used to compute the biases between the GCM and the ocean and atmospheric reanalyses used to force IBI-ERAi. The applied corrections have therefore been well integrated into the model as results for the 1993-2014 period are

370   close to those of IBI-ERAi especially for the steric and manometric SL components. Some thermosteric and halosteric biases still exist in IBI-CCS_corr (Fig. 3d, first and second column) in the BoB (Fig. 1). These biases are related to the Mediterranean waters outflow which does not occur at exactly the same depth or with the same characteristics in IBI-CCS_corr and IBI-ERAi as shown in the TS diagram in Sect. 3.1.3 (Fig. 5).

3.1.2 Circulation

375   **Surface Circulation**
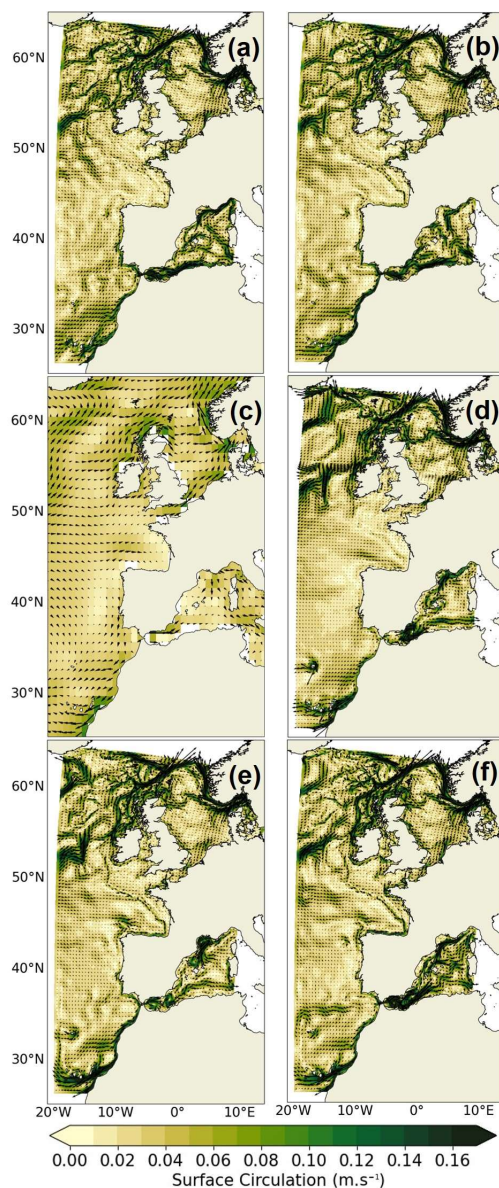
Figure 4: Surface circulation (in m.s^{-1}) over the 1993-2014 period in (a) IBIRYS (b) IBI-ERAi (c) CNRM-CM6-1 (d) CNRM-CM6-1-HR (e) IBI-CCS_raw and (f) IBI-CCS_corr simulations.

380   The general ocean surface circulation averaged over 1993-2014 is illustrated in Fig. 4. The main regional surface dynamical features described in Maraldi et al., 2013; Sotillo et al., 2015 and captured in IBIRYS (Fig. 4a) and IBI-ERAi (Fig. 4b) are also represented in all GCM and RCM simulations. In the Atlantic Ocean, the NAC (Fig. 1) enters the IBI zone at 52°N on the western boundary and separates into several branches with the main one flowing eastward north of the United Kingdom. The NwCC (Fig. 1) in the North Sea and along the Norwegian coasts, the CaC (Fig. 1) along the Moroccan coasts are other

385   mains currents correctly simulated by the GCMs and RCMs. The GCM CNRM-CM6-1-HR and regional simulations show the LPC (Fig. 1) flowing westward along the northern continental shelf in the Mediterranean Sea. However, owing to the large biases of temperature and salinity found in both GCMs in the Mediterranean Sea (Sect. 3.1.1 and Supplementary

Materials Fig. S1 and Fig. S2), the surface circulation cannot be considered realistic in the basin in the corresponding simulations (Fig. 4c,d).

390

When comparing Fig. 4c and d, the impact of the increased resolution between the two GCMs is clear. Thanks to its higher ocean model resolution, CNRM-CM6-1-HR shows a more realistic regional circulation than the 1 ° GCM CNRM-CM6-1. The impact of the DD would therefore be significantly higher using a 1 ° typical CMIP resolution ocean model to force the RCM. However, the dynamically downscaled simulations (Fig. 4e,f) add even more spatial information compared to the

395   GCM CNRM-CM6-1-HR (Fig. 4d). One of the major improvements in the IBI-CCS simulations is the emergence of an additional NAC branch at 48° N, south of the major NAC branch, as in the reference simulations (Fig. 4a,b). Another added value of the DD is seen with the poleward slope currents from the Iberian coasts up to Ireland which do not exist in the GCM simulations. Along the Iberian coasts, where the southward PC and the northward IPC (Fig. 1) co-exit (Cordeiro et al., 2018), the GCMs show no clear feature. Conversely, both the IBI-CCS_raw and IBI-CCS_corr simulations exhibit the PC and IPC currents. These two currents are also found in IBI-ERAi with approximately the same amplitude, but not in the

400   reanalysis IBIRYS for the IPC. Finally, the gyre in the AS (Fig. 1), just east of Gibraltar Strait, is represented in the regionally downscaled simulations but not in the GCMs.

IBI-CCS_corr and IBI-CCS_raw are now compared to assess the impact of bias corrections on the surface circulation (Fig.

405   4e,f). The major difference is the apparition in IBI-CCS_corr of the eastern branch of the AC (Fig. 1) at 35°N with a southward recirculation, as in the reference IBI-ERAi simulation. Another difference between IBI-CCS_corr and IBI-CCS_raw is the strengthening of the NAC branch at 48° N in the corrected simulation leading to a current closer to IBIRYS and IBI-ERAi. In the Mediterranean Sea, large differences between the IBI-CCS_corr and IBI-CCS_raw simulations are also found with a strengthening of the circulation in IBI-CCS_corr.

410

Transport through Gibraltar Strait

Model/Simulation	Period	Inflow transport	Outflow transport	Net transport
IBI-ERAi	1993-2014	1.06 Sv	-0.46 Sv	+0.60 Sv
IBIRYS	1993-2014	1.13 Sv	-0.50 Sv	+0.63 Sv
CNRM-CM6-1-HR	1993-2014	0.54 Sv	-0.55 Sv	-0.04 Sv
IBI-CCS_raw	1993-2014	0.40 Sv	-0.10 Sv	+0.30 Sv
IBI-CCS_corr	1993-2014	0.76 Sv	-0.70 Sv	+ 0.06 Sv
Soto-Navarro et al., 2010	2004-2009	0.81 Sv	-0.78 Sv	+0.04 Sv
Soto-Navarro et al., 2015	2004-2007			+0.05 Sv
Adloff et al., 2015	1961-1990	0.85 Sv	-0.80 Sv	+0.05 Sv

Table 3: Transport through Gibraltar Strait in the different simulations in comparison to previous studies. Transports are positive
415   eastward.

As explained in Sect. 2.2.2, realistic exchanges through Gibraltar Strait have a strong influence on water mass properties and thus on SL over the north-eastern Atlantic region. The values of net transport are presented for CNRM-CM6-1-HR and regional simulations in Table 3 and compared to estimates by Soto-Navarro et al., 2010, 2015; Adloff et al., 2015. Results

420   must be taken with caution as the computation of the fluxes was performed offline (Soto-Navarro et al., 2020). In IBIRYS, the inflow transport (from Atlantic Ocean to Mediterranean Sea) through Gibraltar Strait is overestimated, while the outflow transport (from Mediterranean Sea to Atlantic Ocean) is underestimated. The resulting net transport is largely overestimated

(Table 3 and CMEMS-IBI-QUID-005-002.pdf (copernicus.eu)). In the GCM and IBI-CCS_raw simulations, both inflow and outflow transports are too weak. It is consistent with the surface circulation (Fig. 4) where the entering current at Gibraltar

425 Strait in the GCM and IBI-CCS_raw simulations is weaker than in the reanalysis. The values of the net transport in the IBI-CCS_raw and GCM simulations are different and are not comparable to the estimates by Soto-Navarro et al., 2010, 2015; Adloff et al., 2015. On the contrary, in IBI-CCS_corr, thanks to the SSH tuning applied at the Mediterranean boundary (Sect. 2.2.2), the net transport, inflow and outflow transports are close to the estimates by Soto-Navarro et al., 2010, 2015; Adloff et al., 2015 with a value of +0.06 Sv for the net transport (Table 3).

430 **3.1.3 Water masses properties**
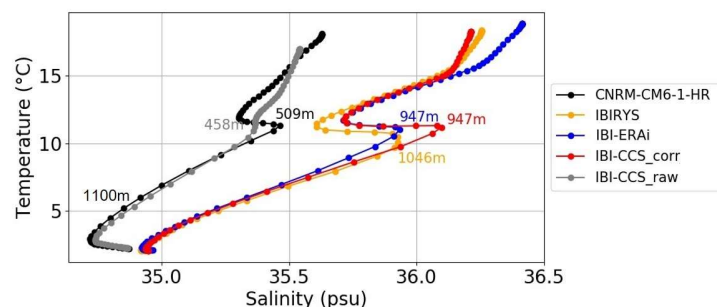
Figure 5: TS diagram performed at the star location of Fig. 1 over the 1993-2014 period for the CNRM-CM-1-HR, IBIRYS, IBI-ERAi, IBI-CCS_corr, IBI-CCS_raw simulations.

The impact of bias corrections for the representation of the Mediterranean water mass properties in the Atlantic Ocean is

435 now assessed. Figure 5 compares the water mass thermohaline properties in the Atlantic Ocean west of Gibraltar Strait for the GCM, IBI-CCS_raw and IBI-CCS_corr simulations to the IBIRYS and IBI-ERAi simulations. The location of the TS diagram (star location of Fig. 1) has been chosen far enough from the western frontier of the domain and in an area where the Mediterranean Outflow Water (MOW) has spread at a depth of around 1100 m (Bozec et al., 2011). Owing to the large surface biases in temperature and salinity found in the GCM and IBI-CCS_raw in the Mediterranean Sea (Sect. 3.1.1 and

440 Supplementary Materials Fig. S1 and Fig. S2), the water mass properties at Gibraltar Strait, and hence of the MOW, cannot be properly modeled. Indeed, large biases are found in the Atlantic Ocean at the MOW depth: biases in temperature and salinity at 1100 m depth reach 4.5 °C and 1.5 psu respectively (Fig. 5). On the contrary, in IBI-CCS_corr where bias corrections are applied, the model is able to reproduce the transformation of fresh and warm surface Atlantic waters into dense and salty MOW leading to a strong reduction of T/S biases (Fig. 5). In IBI-CCS_corr, MOW spreads westward at a

445 depth of 950 m, in good agreement with IBI-ERAi and IBIRYS (Fig. 5). This indicates that bias corrections could lead to a change in the TS diagram shape and water mass characteristics, particularly for the initially biased MOW and not only to a shift in temperature and salinity. Comparisons of 10-yr simulations with the two different river runoff forcings (Sect. 2.2.2) and with or without the SSH tuning in the Mediterranean Sea (Sect. 2.2.2) show that improvements in the T/S diagram are mostly due to the bias corrections (not shown). Thanks to the bias corrections, the water mass characteristics have been

450 corrected thus controlling the influence of the Mediterranean Sea on the Atlantic Ocean and preventing the propagation of the Mediterranean biases into the Atlantic Ocean.

3.1.4 Mean Sea Surface Height
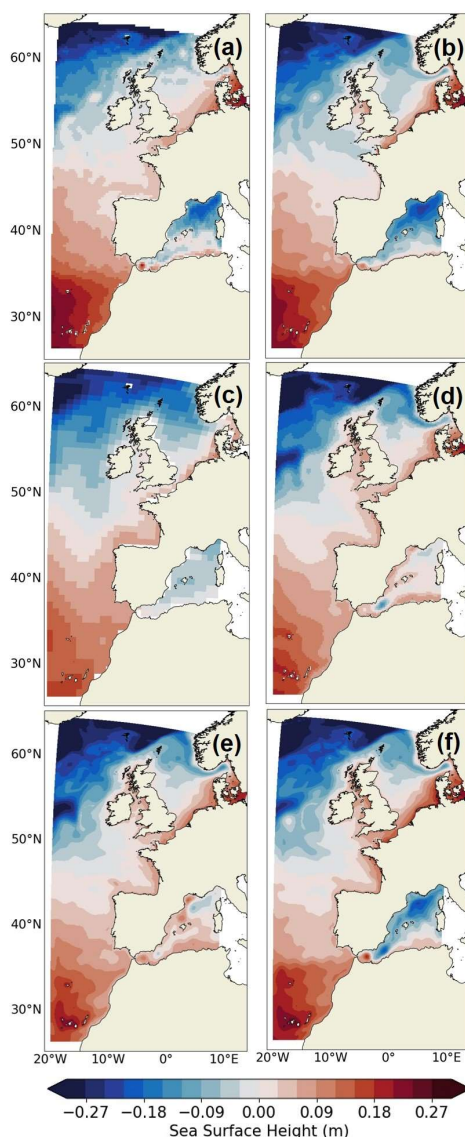
Figure 6: Mean sea surface height over the 1993-2014 period in (a) MDT CNES-CLS-18 (b) IBI-ERAi (c) CNRM-CM6-1 (d)
455   **CNRM-CM6-1-HR (e) IBI-CCS_raw and (f) IBI-CCS_corr.**

The mean dynamic topography (MDT) gives the time mean sea surface height above the geoid due to ocean circulations. The
dataset of reference for the MDT for the 1993-2012 period is the CNES CLS18 data set (Mulet et al., 2021). The CNES
CLS18 MDT has a 1/8° resolution and is based on GOCE and GRACE data, altimetry and in-situ data, as well as on the
GOCO05S geoid model. The observed MDT is comparable to the modeled time mean SL called in this section the mean sea
460   surface height (MSSH).

Figure 6 compares the CNES CLS18 MDT to the MSSH for the different simulations. In all simulations, the Atlantic MSSH
matches well the observed MDT (Fig. 6a). Indeed, the Atlantic MSSH northwest to southeast gradient associated to the NAC
(Fig. 1), subtropical and subpolar gyres is well reproduced in all the GCM and IBI-CCS simulations in comparison to the

465 observations and IBI-ERAi (Fig. 6). Along the NS (Fig. 1) and eastern EC (Fig. 1) coasts, all GCM and IBI-CCS simulations show elevated MSSH similar to the observations and IBI-ERAi simulation. However, in the BoB (Fig.1), GCM and IBI-CCS simulations show a too elevated MSSH compared to observations and IBI-ERAi simulation (Fig. 6).

As for the surface circulation in Sect. 3.1.2, the impact of the increased resolution between the two GCMs (Fig. 6c,d) is
470 clear, with more spatial information for the MSSH in CNRM-CM6-1-HR. Compared to CNRM-CM6-1-HR (Fig. 6d), the even higher resolution in IBI-CSS_raw (Fig. 6e) only slightly improves the MSSH in some coastal areas like the CS (Fig. 1), IS (Fig. 1) and western part of the EC.

The bias corrections applied in IBI-CCS_corr (Fig. 6f) improve the excessively low MSSH pattern at 53° N of the western
475 boundary found in CNRM-CM6-1-HR and IBI-CCS_raw (Fig. 6d,e). The bias corrections also have a large impact in the Mediterranean Sea where the GCM CNRM-CM6-1-HR and IBI-CCS_raw MSSH is overestimated. Indeed, in these simulations Atlantic waters flowing through Gibraltar Strait then flow northward toward the Balearic Islands and the Gulf of Lion, which is unrealistic according to observations and previous studies (Adloff et al., 2018). On the contrary, in IBI-CCS_corr where bias corrections are applied, Atlantic waters are trapped in the Alboran gyre and then stick to the north
480 African coast, as in the observed MDT and IBI-ERAi (Fig. 6). In the northern Mediterranean Sea, the low SL feature associated with the large gyre in the convection area of the Gulf of Lion is also well represented in IBI-CCS_corr in comparison to the MDT and IBI-ERAi.

3.1.5 SL interannual variability
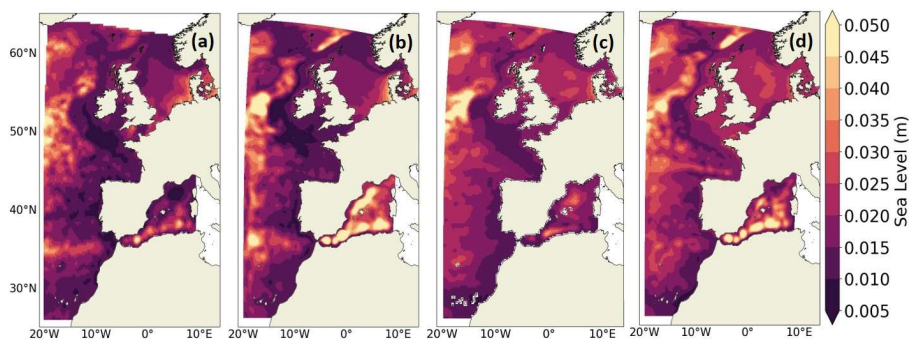
485 **Figure 7: SL interannual variability over the 1993-2014 period in (a) altimetry (b) IBI-ERAi (c) CNRM-CM6-1-HR and (d) IBI-CCS_corr. The interannual variability is computed as the standard deviation of the detrended annual mean SL.**

Here, the CNRM-CM6-1-HR and IBI-CCS_corr simulations are compared to the global gridded reprocessed SEALEVEL_GLO_PHY_L4_REP_OBSERVATIONS_008_047 altimetric observation product distributed by CMEMS. The product is provided at a 0.25 ° resolution since 1993 and is based on the combination of measurements from different
490 altimeter missions (https://catalogue.marine.copernicus.eu/documents/QUID/CMEMS-SL-QUID-008-032-062.pdf and https://catalogue.marine.copernicus.eu/documents/PUM/CMEMS-SL-PUM-008-032-062.pdf).

The large SL interannual variability associated with the main currents of the zone such as the NAC, AC, AlC, LPC of Fig. 1 is well represented in IBI-CCS_corr (Fig. 7d), as shown by comparison with the altimetry product and IBI-ERAi (Fig. 7a, b).
495 On the large continental shelf, the GCM and RCM both simulate a larger interannual variability than the altimetry product except in the German Bight. Indeed, in the German Bight and north of the Netherlands, the altimetry product and IBI-ERAi

show a relatively large interannual variability which is not present in CNRM-CM6-1-HR and IBI-CCS_corr. In both regional IBI-CCS_corr and IBI-ERAi simulations, the interannual variability in the Mediterranean Sea is very large which is not the case in the GCM simulation and to a lesser extent in the altimetric product (Fig. 7).

500

3.1.6 Extreme SLs
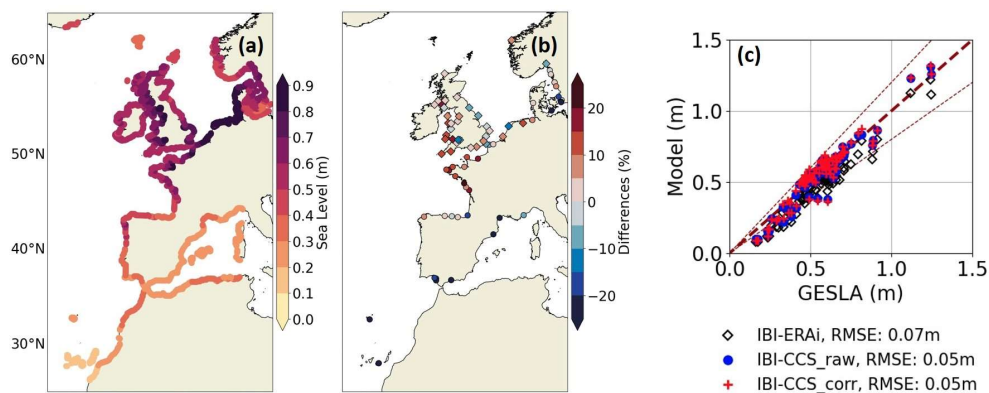
Figure 8: (a) Non-tidal residuals 99th percentile values over the 1993-2014 period in IBI-CCS_corr. (b) Relative error of the non-tidal residuals 99th percentile of IBI-CCS_corr compared to GESLA TG data over the 1993-2014 period. Circles represent TG
505 **data at 1-hour frequency and the diamonds stand for TG data at higher frequency. (c) Scatter plot of simulated vs observed 99th percentile at TG stations in IBI-ERAi (white diamonds), IBI-CCS_raw (blue circles) and IBI-CCS_corr (red cross). The thin dark red dashed lines indicate the 20% error margin.**

For impact studies, it is even more crucial to get a good representation of SL extreme values. Extreme SLs of the IBI-
510 CCS_raw and IBI-CCS_corr simulations are thus validated against tide gauge (TG) records and IBI-ERAi. The GESLA (Global Extreme Sea Level Analysis GESLAv2) dataset provides high-frequency (at least hourly) TG data records (Woodworth et al., 2017). The selected TG stations have a temporal data coverage of no less than 75% over the 1993-2014 period and are marked with red dots in Fig. 1.

515 Extreme SLs are investigated here with the 99th percentile based on hourly averaged outputs of the IBI-CCS model. GCM CNRM-CM6-1-HR did not produce sufficiently high frequency outputs to assess such SL extreme events. In addition, CNRM-CM6-1-HR is not able to properly represent SL extremes as these are highly related to tides which are not represented in this model. Therefore, the explicit representation of processes like tides is an important added value of the regional model. IBI-CCS and the IBIRYS reanalysis are based on the same configuration, including tides implementation
520 which has been validated in CMEMS-IBI-QUID-005-002.pdf (copernicus.eu) and Maraldi et al., 2013. Thus, the comparison rather focuses here on the validation of non-tidal residuals (where tides are filtered from the SL time series). During extreme SL events, non-tidal residuals are dominated by atmospheric/storm surges.

Figure 8 shows that the non-tidal residuals 99th percentile in IBI-CCS_raw and IBI-CCS_corr is properly represented in
525 comparison to TG data. Both IBI-CCS_raw and IBI-CCS_corr show performances similar to, but slightly better than those of the reference simulation IBI-ERAi. Indeed, the error at the different TG stations rarely exceeds 20% (Fig. 8c) and the RMSE do not exceed 5 cm. The largest errors are found on the southern part of the domain where the 99th percentile of non-tidal residuals are the smallest. In conclusion, thanks to the coastal processes included and high frequency outputs of the RCM, the regional simulations are able to properly model extreme SLs.

530 **3.2 Regional projections under climate change scenarios with a focus on SL**

Here, the regional projections are presented for the SSP5-8.5 and SSP1-2.6 scenarios for the different variables validated in the former section. Additionally, the effect of DD and of bias corrections on the projections is assessed with a focus on SL changes.

3.2.1 Projected trend of regional mean total SL
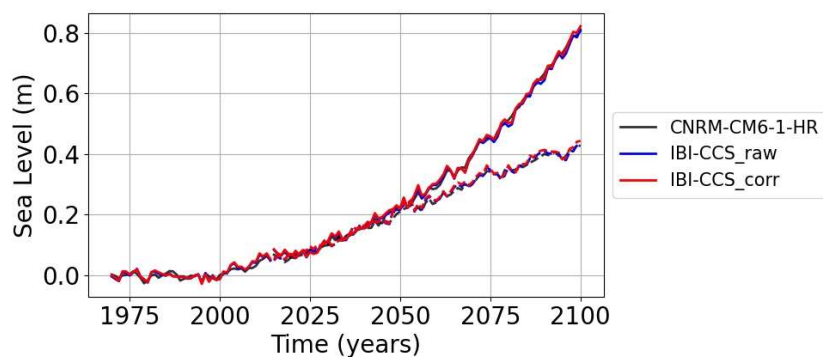
535

Figure 9: Time series of annual mean SL changes (in m) averaged over the IBI domain for the historical period (1970-2014), SSP5-8.5 (solid line) and SSP1-2.6 (dashed line) scenarios (referenced to 1986-2005) for the GCM and the two regionally downscaled IBI-CCS_raw and IBI-CCS_corr simulations.

In Fig. 9, the historical and projected mean SL changes over the whole IBI domain are assessed for the SSP5-8.5 and SSP1-
540   2.6 scenarios for the GCM and downscaled simulations. As explained in Sect. 2.3.3, none of the GCM and regionally
downscaled simulations represent the spatial mean thermosteric effect on SL. It has thus been computed and added a
posteriori. By the end of the century, a mean SL increase of +80 cm is simulated over the IBI domain for the SSP5-8.5
scenario (relative to 1986-2005) and +40 cm for the SSP1-2.6 scenario. These values are close to the GMSL projections of
+71 cm (RCP8.5) and +39 cm (RCP2.6) from Oppenheimer et al., 2019 over the same period. In Fig. 9, the consistency of
545   the trend of total regional mean SL between the global and regional simulations for the two scenarios validates the DD
technique employed. It assesses that bias corrections do not impact the projected mean SL trend for both scenarios.

3.2.2 Projected changes in surface circulation
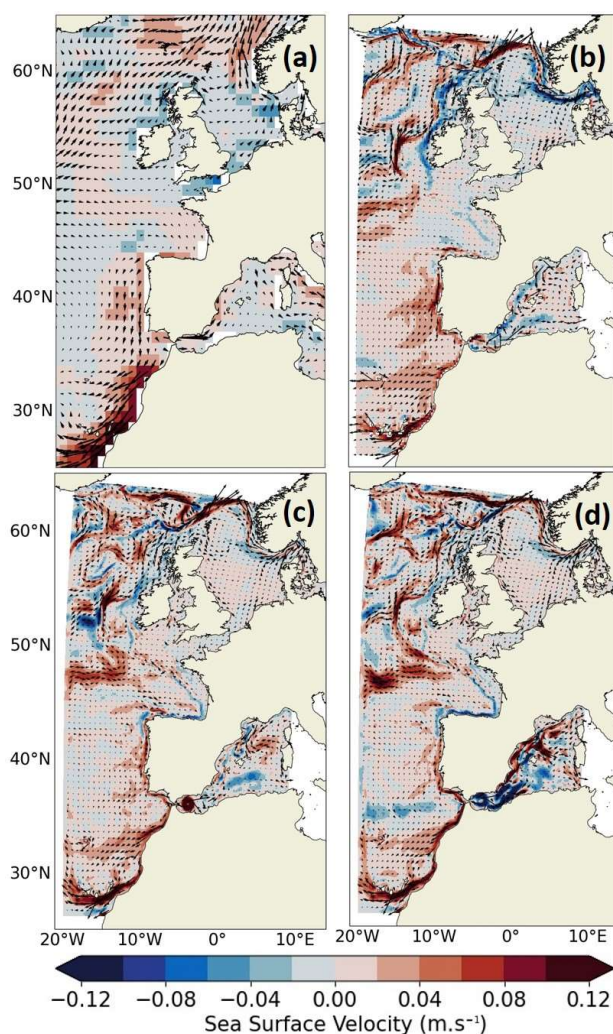
**Figure 10: Projected changes in surface ocean currents (in m.s⁻¹) for the 2081-2100 period (relative to 1986-2005) under the SSP5-
550   8.5 scenario for (a) CNRM-CM6-1 (b) CNRM-CM6-1-HR (c) IBI-CCS_raw and (d) IBI-CCS_corr. The magnitude of surface
currents changes is indicated by the color shading.**

Figure 10 shows projected changes in ocean surface currents under the SSP5-8.5 scenario in the two GCMs, IBI-CCS_raw and IBI-CCS_corr simulations. Projected changes generally agree well between the GCM and RCM simulations in terms of

555 patterns, except in the Mediterranean Sea. While all the simulations show a strong intensification of the PC and CaC (Fig. 1), projected changes exhibit larger amplitudes in CNRM-CM6-1-HR (Fig. 10b) and IBI-CCS (Fig. 10c,d) than in CNRM-CM6-1 (Fig. 10a) thanks to their higher resolution. Indeed, in CNRM-CM6-1-HR and IBI-CCS, large changes are found in the north of the domain with a strengthening of the branch of the NAC (Fig. 1) around 48°N. The GCM also projects a strong decline of the NwCC and in the NAC branch flowing around the United Kingdom (Fig. 10b) which is not modeled in

560 the RCM simulations (Fig. 10c,d). In both IBI-CCS simulations, the higher resolution adds more spatial information to the projections such as the decline of the poleward current from Iberia to Ireland (Fig. 10c,d). In the Mediterranean Sea, the four simulations show very different changes. Results have to be taken with caution as the surface circulation of the historical simulations are not very realistic in the Mediterranean Sea. In the Mediterranean Sea, projected changes in the surface circulation are small in the GCMs and IBI-CCS_raw whereas in IBI-CCS_corr, the projected changes are substantial and

565 show a strong weakening of the Alboran gyre (Fig. 10d). In conclusion, both the impact of the resolution and bias corrections on the surface circulation projected changes are substantial.

3.2.3 Water mass properties projections
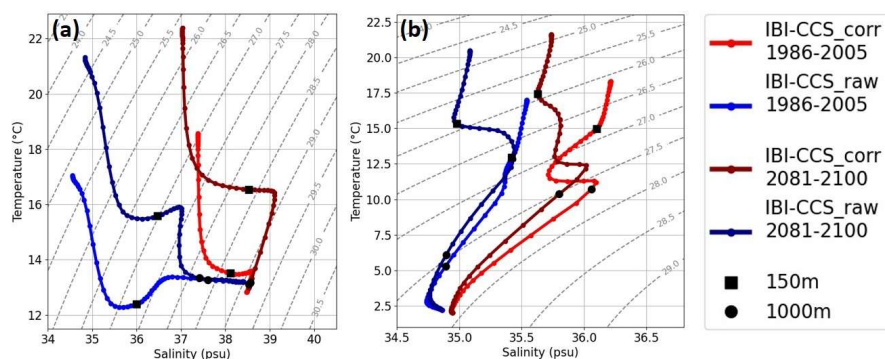
Figure 11: TS diagram for the SSP5-8.5 scenario for the present (1986–2005) (light line) and future (2081–2100) (dark line) periods
570 **for IBI-CCS_corr (red) and IBI-CCS_raw (blue) (a) in the western Mediterranean Sea (b) in the BoB.**

The historical and projected changes of the water mass properties east and west of Gibraltar Strait are presented with a TS diagram in Fig. 11. Projections of the water masses TS characteristics in the western Mediterranean Sea (Fig. 11a) are in close agreement with those of Soto-Navarro et al., 2020 in IBI-CCS_corr whereas projections from IBI-CCS_raw are totally out of the range of the 20 CMIP models used in Soto-Navarro et al., 2020. Indeed, IBI-CCS_corr displays a strong warming

575 of the upper 1000 m with a general decrease in density and also an abrupt change in the TS characteristics of intermediate and deep waters. These results provide more confidence in the IBI-CCS_corr simulation.

The second TS diagram (Fig. 11b) is performed in the BoB (Atlantic Ocean, at the star location of Fig. 1). IBI-CCS_corr projections show a general warming and freshening of the water column. MOW flowing westward in the Atlantic Ocean

580 seem to be found at shallower depths at the end of the 21st century. When comparing the projections of IBI-CCS_raw and IBI-CCS_corr at a depth of 1000 m (black dots in Fig. 11b), IBI-CCS_corr exhibits a freshening whereas IBI-CCS raw does not show a particular change. This result confirms these of Sect. 3.1.3: bias corrections could lead to a change in the TS diagram shape. Although the bias corrections of temperature and salinity are stationary, the projected changes in the TS diagrams of the regional simulations with and without corrections are not the same and thus depend on the mean state. Bias

585 corrections can therefore be important for projected water mass changes through the water column.

3.2.4 Projected changes of SL components
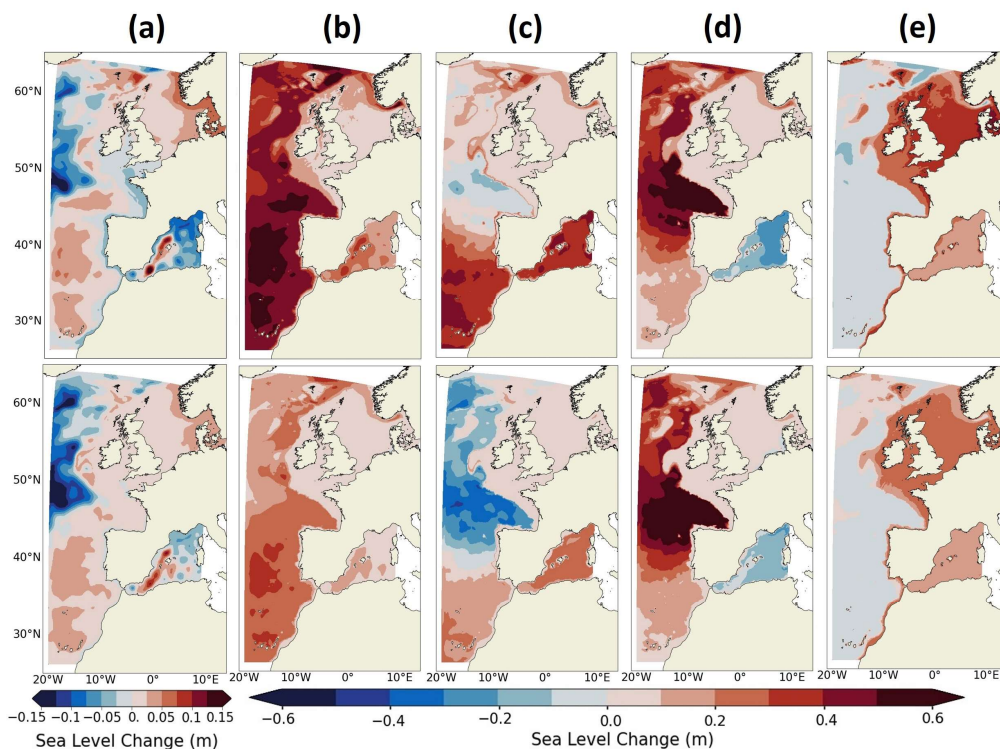
Figure 12: Projected changes (2081-2100 vs 1986-2005) under the SSP5-8.5 (upper row) and SSP1-2.6 (lower row) scenarios in the IBI-CCS_corr simulation for the (a) DSL, (b) steric, (c) thermosteric (d) halosteric and (e) manometric SL components. The steric, thermosteric and halosteric SL components have been computed between 0-2000m depth. Note that the DSL mean over the IBI zone is 0.

Figure 12 shows the projected changes of SL components described in Sect. 2.3 for SSP5-8.5 and SSP1-2.6 scenarios for the IBI-CCS_corr regional simulation. For all the SL components, spatial patterns of projected changes are quite similar under the two scenarios. Indeed, for the DSL changes, both scenarios exhibit an increase of the DSL in the North Sea and a decrease in the north-western part of the domain (Fig. 12a). The main difference between both scenarios is the projected slight fall of the DSL in the BoB under SSP5-8.5 which is not projected under the SSP1-2.6 scenario. Figure 12b shows a large steric SLR in the deep ocean compared to the shelf, as expected for this depth-integrated variable. This result is consistent with Fox-Kemper et al., 2021. The corresponding steric SL gradients are compensated by shelf mass loading (Richter et al., 2013). Figure 12e indeed shows a slight decrease of manometric SL in the deep ocean and a substantial manometric SLR over the shelf. In general, steric and manometric SL changes are of smaller amplitude under SSP1-2.6 than under SSP5-8.5. Thermosteric SL is projected to increase south of around 40°N and in the Mediterranean Sea but to decrease in the deep ocean north of 40°N, especially under SSP1-2.6 (Fig. 12c). This pattern is inherited from the GCM forcing at the boundaries. A smaller projected decrease in thermosteric SL in the north-western part of the domain has also been observed in Hermans et al., 2020 with the MPI-ESM-LR GCM. The projected warming in the Mediterranean Sea is consistent with Adloff et al., 2015; Soto-Navarro et al., 2020. Both scenarios exhibit an increase of halosteric SL in the Atlantic Ocean contrary to Hermans et al., 2020, and a decrease in the Mediterranean Sea (Fig. 12d). For the Mediterranean Sea, it seems there is no clear feature in salinity projected changes in the different simulations from Soto-Navarro et al., 2020. Moreover,

3.2.5 Impact of the resolution for the regional projections of SL
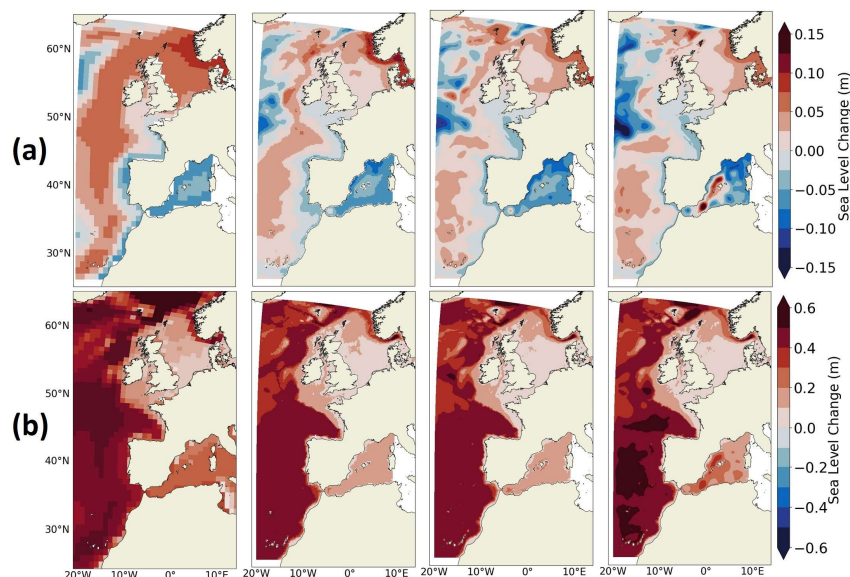
Figure 13: Projected changes (2081-2100 vs 1986-2005) in (a) DSL and (b) steric SL over 0-2000 m depth under the SSP5-8.5 scenario in CNRM-CM6-1 (first column), CNRM-CM6-1-HR (second column), IBI-CCS_raw (third column) and IBI-CCS_corr (last column) simulations. Note that the DSL mean over the IBI zone is 0 in the RCMs and thus, to compare the DSL between the GCMs and RCMs, the mean DSL over the IBI domain is removed from the GCMs.

Figure 13 compares the projected changes in DSL and steric SL in both GCMs and RCMs under the SSP5-8.5 scenario to assess the impact of the resolution on SL projected changes. The spatial patterns of steric SL projected changes are very similar for all the simulations (Fig. 13b) and agree with global projections from Fox-Kemper et al., 2021 and regional projections from Hermans et al., 2020. For DSL changes (Fig. 13a), the different simulations agree well with a projected increase of the DSL in the North and Baltic Seas, especially off the coasts of Scandinavia. Close to the western boundary, a decrease in DSL is projected in all simulations north of around 50° N (Fig. 13a). In the Mediterranean Sea, each simulation shows different projected DSL and steric SL changes (Fig. 13a,b). Globally, the projected changes spatial pattern of steric SL and more importantly of DSL in CNRM-CM6-1-HR and IBI-CCS have significantly more spatial information at the coast compared to the lower resolution CNRM-CM6-1. In addition, the added value of the high resolution GCM and regional simulations compared to the GCM CNRM-CM6-1 appears on the steric SL changes where strong gradients of bathymetry are found.
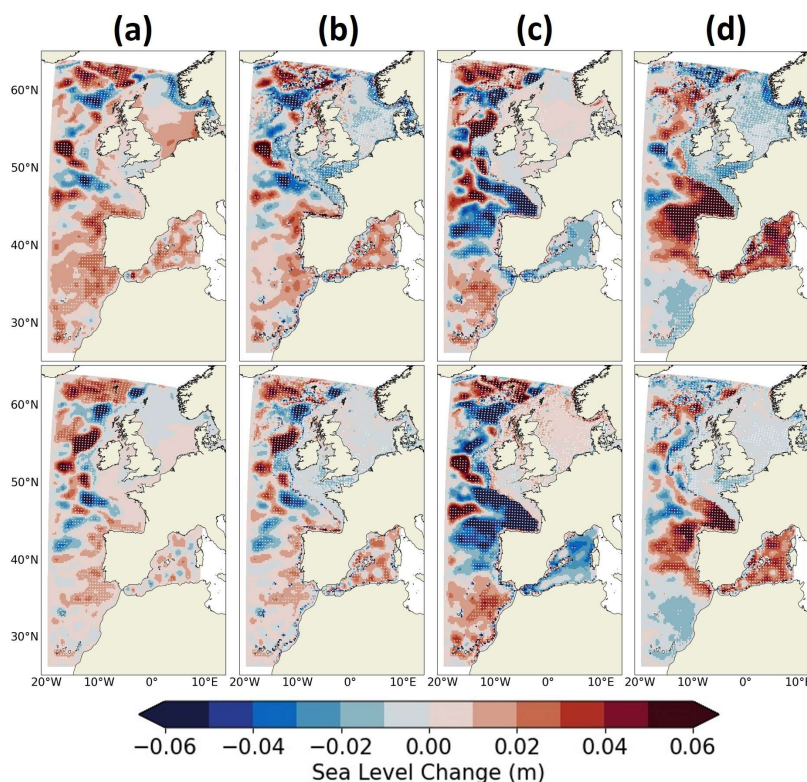
Figure 14: Differences of projected changes (2081-2100 vs 1986-2005) under the SSP5-8.5 (upper row) and SSP1-2.6 (lower row) scenarios between CNRM-CM6-1-HR and IBI-CCS_raw for the (a) DSL without IB effect, (b) steric, (c) thermosteric and (d) halosteric SL components. The steric, thermosteric and halosteric SL components have been computed between 0-2000 m depth. The differences have been computed on the GCM grid. A student test has been performed with a confidence interval of 95% and the significant differences between the two simulations have been marked with white dots.

To isolate the impact of resolution on the projected changes, Figure 14 shows the differences in SL drivers' projected changes between the regionally downscaled IBI-CCS_raw and the global CNRM-CM6-1-HR. The comparisons allow us to assess the impact of the increased model resolution for the projections of the different SL components. The consistency of the changes between the 2 scenarios suggests a robust climate change signal rather than a signal dominated by internal climate variability (Fig. 14). Differences in projected DSL changes due to a higher resolution are generally more important for the SSP5-8.5 than for the SSP1-2.6 scenario.

In coastal zones, the largest differences in projected DSL are found along the Norwegian coasts, with a 5cm smaller projected change in the IBI-CCS_raw simulation compared to the GCM under SSP5-8.5 (Fig. 14a). This difference is related to the strong decrease in the surface circulation of the NwCC (Fig. 1) in the GCM but not in the RCM (Fig. 10). Substantial differences in projected DSL changes are also found around Iberia (Fig. 14a) and are mostly related to differences in halosteric SL projected changes which are partly compensated by differences in thermosteric projected changes (Fig. 14c,d). Otherwise, differences in projected changes in DSL between the GCM and IBI-CCS_raw are rather small in coastal areas, which is due to the relatively high resolution of the GCM and in particular of its bathymetry and land mask. This is consistent with the findings of Hermans et al., 2020 where a larger impact of increased resolution through dynamic downscaling was found as they used coarser GCMs. They have highlighted the importance of a realistic bathymetry and land mask for SL projections. Moreover, the impact of the higher resolution is rather small due to the peculiarities of the region as the IBI zone includes many continental shelves. In shallow regions such as continental shelves, the Rossby radius is smaller

than in the surrounding deep ocean which requests an even higher resolution to resolve mesoscale processes. Over the north-western European continental shelf, a resolution of at least 1/50 ° is required for ocean models to be eddy resolving, while models at 1/12 ° are eddy resolving in the deep part of the Atlantic domain in IBI (Hallberg, 2013). The RCM is therefore

655 eddy-resolving in the deep Atlantic part of the domain, while the GCM is only eddy-permitting. The small differences in coastal steric, thermosteric and halosteric SL projected changes are consistent with the DSL changes at the coast (Fig. 14b,c,d). In the deep ocean and particularly in the north-western part of the domain, where the surface circulation changes are the most important, differences between the GCM and RCM largely exceed the differences on the shelf for both scenarios and for all the SL components but their spatial patterns are rather noisy (Fig. 14).

660 **3.2.6 Impact of bias corrections on regional projections of SL**
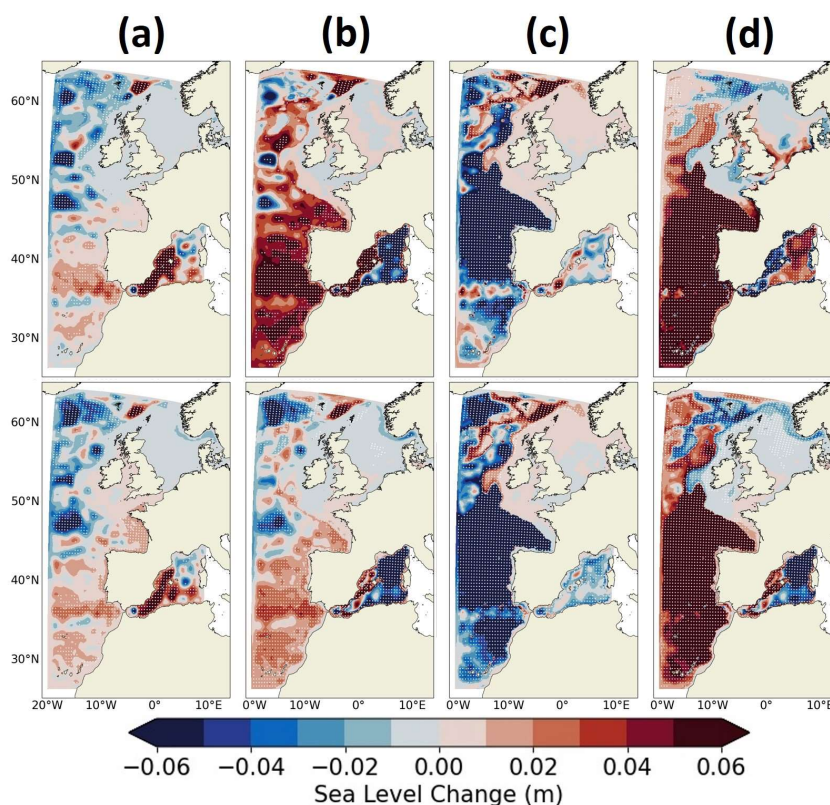
Figure 15: Differences of projected changes (2081-2100 vs 1986-2005) between IBI-CCS_corr and IBI-CCS_raw simulations for the DSL (first column), the steric (second column), thermosteric (third column) and halosteric (last column) SL components under the SSP5-8.5 (upper row) and SSP1-2.6 (lower row) scenarios. The steric, thermosteric and halosteric SL components have been
665 **computed between 0-2000 m depth. A student test has been performed with a confidence interval of 95% and the significant differences between the two simulations have been marked with white dots.**

The impact of bias corrections on SL projections are now investigated by comparing projected SL changes between IBI-CCS_corr and IBI-CCS_raw (Table 1). The spatial patterns of the differences between the projected changes of IBI-CCS_raw and IBI-CSS_corr are very similar for all the SL components and scenarios, except in the Mediterranean Sea (Fig.
670 15). In general, large differences in projected SL changes between the two simulations are found in the deep ocean, the impact of bias corrections in coastal areas being small for both scenarios and for all the SL components.

In this section, the focus is done on the DSL changes (Fig. 15a). Differences in DSL changes in the deep ocean seem to be independent of the climate change scenario (Fig. 15a). In the north-western part of the IBI domain where the surface

675 circulation changes are the most important, the projected DSL changes are up to 10 cm smaller in IBI-CCS_corr (Fig. 15a). In the Mediterranean Sea where the bias corrections are substantial, differences in DSL changes are up to 15 cm larger in IBI-CCS_corr compared to IBI-CCS_raw in the Alboran Sea associated with a larger increase in the net transport through Gibraltar Strait (not shown here). Also, the Alboran gyre is projected to decrease in IBI-CCS_corr under both climate change scenarios whereas it is projected to strengthen in IBI-CCS_raw (Fig. 15a and Fig. 13a). Impacts of bias corrections in

680 coastal areas are rather small for the SSP5-8.5 scenario (except in the Mediterranean Sea) and are larger for the SSP1-2.6 scenario (Fig. 15a). For instance, the projected DSL changes in the SSP1-2.6 scenario is up to 2 cm larger in IBI-CCS_corr compared to IBI-CCS_raw in the BoB and along the Iberian coasts, which is of similar amplitude to the projected DSL change in IBI-CCS_corr. Because of the stationarity of bias corrections, their impact on projected changes is larger when the climate change signal is smaller.

685 **3.2.7 Projected changes of SL interannual variability**
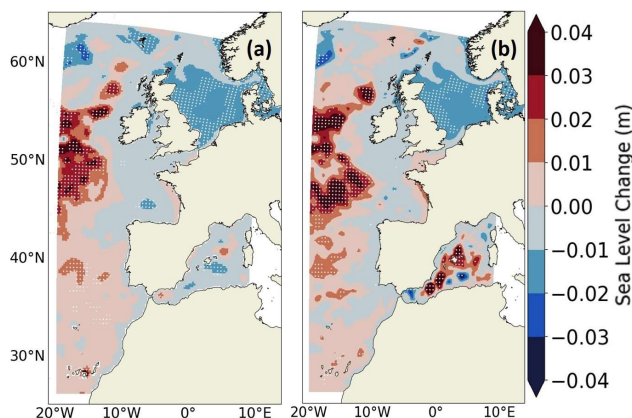
Figure 16: Projected changes (2081-2100 vs 1986-2005) of SL interannual variability under the SSP5-8.5 scenario for the (a) GCM CNRM-CM6-1-HR and (b) IBI-CCS_corr. The interannual variability is computed as the standard deviation of the detrended annual mean SL. A Fisher test has been performed with a confidence interval of 90% and the significant differences between the
690 **two simulations have been marked with white dots.**

Figure 16 shows the projected changes of SL interannual variability under the SSP5-8.5 scenario for the GCM CNRM-CM6-1-HR and for the IBI-CCS_corr regional simulation. Thanks to the bias corrections method used here, the internal variability of the GCM is conserved which allows investigating the projected changes of the variability in the regional simulations. This would not have been possible with other correction methods such as the delta method i.e. mean state change projected

695 anomalies added to historical forcings where the high frequency variability is unchanged between the global and regional models, by construction.

Projected changes in interannual variability are consistent between the GCM and IBI-CCS_corr simulation (Fig. 16). Significant changes in the amplitude of interannual variability are observed where important changes in circulation are also

700 projected (Sect. 3.2.2), e.g. the NAC and in the Mediterranean Sea. Projected changes are also significant in the North Sea shelf in both GCM and IBI-CCS_corr. Figure 16 displays changes in variability but it is not possible to state if these changes are indeed reflecting changes in interannual variability or lower frequency signals such as multi-decadal variability.

3.2.8 Projected changes of extreme SLs
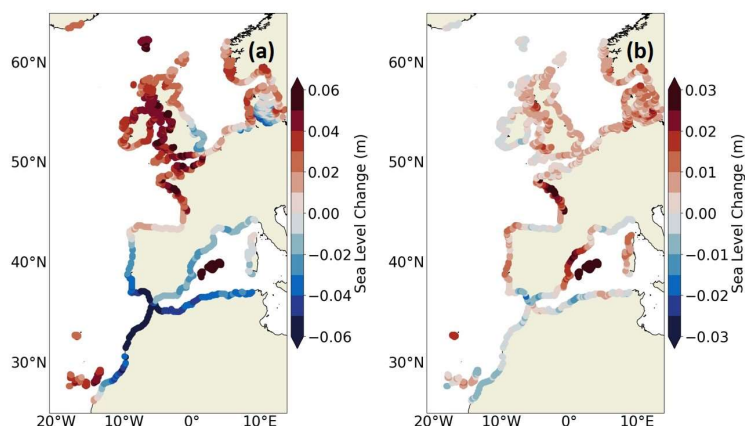
705 **Figure 17: (a) Projected changes of the non-tidal residual 99th percentile for the SSP5-8.5 scenario between 2081-2100 and 1986-2005 period in IBI-CCS_corr. (b) Differences with projected changes in IBI-CCS_raw.**

For impact studies, it is necessary to consider projected SL extreme values. Figure 17 shows the projected changes in the 99th percentile of non-tidal residuals under the SSP5-8.5 scenario. Note that the mean has been subtracted on both time slices 1986-2005 and 2081-2100 to remove SLR effect on extreme SLs and to assess changes in the remaining component

710 which corresponds to the atmospheric surge. Changes in extreme SLs are therefore of a small amplitude of maximum 6 cm (Fig. 17a) as changes in extreme SLs are mainly driven by SLR (Vousdoukas et al., 2018b; Muis et al., 2020). However, some spatial differences are found on the atmospheric surge with an increase in extreme SLs in AS, EC, CS, IS (Fig. 1). The impact of the bias correction on this high-frequency diagnostic is assessed on Fig. 17b. Projected changes of 99th percentile of non-tidal residuals are relatively weakly affected by the bias correction except on the AS (Fig. 1) and in the Mediterranean

715 Sea where the differences with IBI-CCS_raw are half the climate change signal.

3.2.9 Projected changes in the M2 tidal amplitude
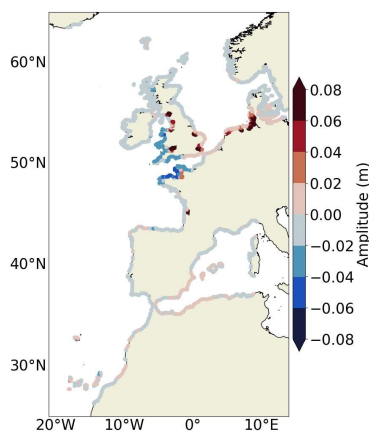
Figure 18: Projected changes of the M2 tidal amplitude for the SSP5-8.5 scenario between 2081-2100 and 1986-2005 period in IBI-
720 **CCS_corr.**

The main added value of the RCM in comparison to the GCM is the inclusion of processes driving SL changes at the coast such as tides (Sect. 2.1.2). Here, the projected changes of the major tidal constituent (M2) amplitude are assessed under the SSP5-8.5 scenario (Fig. 18). These changes in amplitude are important as tides are major drivers of extreme SLs. Projected tidal changes over the 21st century are mostly due to SLR (Fox-Kemper et al., 2021). However, projected changes are not

725 expected to be large in IBI-CCS_corr as the tidal potential imposed at the boundaries of the domain does not change in response to climate change and as coastlines are fixed in the model (no wetting and drying, erosion etc). Nevertheless, tides can be impacted by the SLR on the shelf, far enough from the boundaries. Here, with a SLR of about +80 cm at the end of the century (Sect. 3.2.1), the M2 tidal amplitude seems to be impacted mostly in the southern part of the North Sea on the large continental shelf. In this region, the M2 tidal amplitude is projected to increase by 10%, which is consistent with Idier

730 et al., 2017. Projected changes in M2 phase have also been assessed under the SSP5-8.5 scenario and show no difference compared to the historical simulation and no displacement of the amphidromic points (not shown here).

4 Conclusion

Previous dynamical downscaling studies have provided regional projections of SL based on CMIP5 GCMs (e.g. Hermans et al., 2020; Liu et al., 2016; Zhang et al., 2017; Gomis et al., 2016, Jin et al., 2021). The objective of this study was to provide

735 projections of sea level changes in the north-eastern Atlantic region bordering western Europe, focusing on methodological aspects. To do that, a regional ocean model IBI-CCS is set up to refine the CMIP6 GCM CNRM-CM6-1-HR SL projections using a DD method. To limit the GCM bias propagation into the regional projections, seasonal mean bias corrections have been applied to the GCM outputs before using them to initialize and to force the RCM. To disentangle the respective effects of the pure DD and of introducing bias corrections both on the current climate and on the projected change, different

740 analyses were performed.

Comparisons between the GCM and the regional simulation without bias correction have been performed to assess the impact on the simulations of: (1) the higher resolution and (2) the inclusion of processes driving SL at the coast in the RCM. These comparisons show that the DD method conserves the GCM spatial patterns, its interannual variability and trends. Over

745 the historical period, the 1/12 ° resolution of the regional model IBI-CCS allows for a better regional circulation and SL with more spatial information. However, the impact of the increased resolution on the projections is limited by the ¼ ° high resolution of the GCM associated with a quite realistic bathymetry and land mask. Additionally, the IBI zone concentrates many continental shelves where the Rossby radius is small which requires a resolution of at least 1/50 ° to be eddy resolving. This limits the gain to be expected over continental shelves in the IBI region from the RCM resolution of 1/12 °. We expect

750 that the impact of DD would be much larger if the GCM had a more typical CMIP ocean model resolution of 1 °. The choice of the eddy-permitting high-resolution GCM allows to obtain realistic regional circulation and MSSH which would probably not have been the case with a 1 ° GCM as shown in the comparisons between CNRM-CM6-1-HR and CNRM-CM6-1. Moreover, a higher resolution is also interesting to obtain a less smooth atmospheric forcing which is very important for the modeling of extreme SLs. Thanks to the physical processes included in the RCM that the GCM does not have, like tides and

755 atmospheric pressure forcing, the IBI-CCS simulations are able to correctly represent high-frequency SLs. The validation shown here provides some confidence on the realism of the representation of these processes and paves the way for a future analysis more focused on extreme SLs projected changes.

Other comparisons have been performed to assess the impact of bias corrections on the simulation of ocean properties

760 including SL. Thanks to the bias corrections, the large-scale performances of IBI-CCS are better than those of the GCM in terms of SL components, regional circulation and representation of water masses. For instance, the characteristics of the

water masses were corrected thereby controlling the influence of the initially highly biased Mediterranean Sea on the Atlantic Ocean. For the projected changes, in our case, the corrections have a small impact at the coast in general, except in the Mediterranean Sea where the biases were substantial. Additionally, due to the stationarity of the bias corrections, their impact on projected changes is larger for the SSP1-2.6 scenario where the climate change signal is weaker than for the SSP5-8.5 scenario. This method therefore seems to be applicable to other models even with biases of strong amplitudes. Moreover, although the corrections were stationary, the projections in the water mass properties in the simulations with and without corrections of biases were different for a same depth (different TS diagram shape). Another added value of the bias corrections is that they allow conserving the internal variability of the GCM. The internal variability in the regional model is driven by that of the GCM, for the historical period and projections, therefore allowing to investigate projected changes of the variability in the regional simulations. This would not have been possible with the delta correction method where the GCM projected changes are added to a reference past state.

The use of a single forcing GCM and a single member does not allow to quantify uncertainties of the projected results. Here, the aim of the study was not to characterize the uncertainties or provide a likely range of projected changes over the IBI region. The objective was to use a method to produce climate projections dealing with GCM biases in order to apply the method to a larger number of models in forthcoming studies. More specifically, the regional configuration has been developed to investigate SL changes related questions in the IBI region in terms of processes, not uncertainties. To gain insights on the representativeness of the GCM forcing model chose here, we checked that the GCM was not an outlier of the CMIP6 models for a set of metrics relevant for SL changes on the IBI zone. In a way, the differences in the regional climate change projections with and without applying bias corrections are another indication of the uncertainties in downscaled climate simulations (Hernández-Díaz et al., 2019).

When considering a large number of models, the bias corrections method used here is not systematically applicable, so it is preferable to select the forcing models based on one or several criteria before using them for projections. The best would be to eliminate the models that have strong difficulties in the area considered and for the key variables of the intended study. Emergent constraints methods were also developed to overcome model biases and better characterize the uncertainties of the projections (Chen et al., 2020; Grinsted and Christensen, 2021; Forster et al., 2021).

As a conclusion, in this paper, the IBI-CCS regional model has been shown to be a suitable tool to investigate climate projected changes related questions over the ocean in the IBI region, especially regarding SL. For example, we will be able to analyze the projected changes in extreme SLs.

Code availability

The IBI-CCS model is based on the NEMO 3.6 version developed by the NEMO consortium. All specificities included in the NEMO code version 3.6 are freely available (https://www.nemo-ocean.eu/).

Data availability

Information on CNRM-CM6-1-HR and CNRM-CM6-1 simulations can be found at https://doi.org/10.22033/ESGF/CMIP6.4067 (CNRM-CM6-1-HR, historical), https://doi.org/10.22033/ESGF/CMIP6.4164 (CNRM-CM6-1-HR, piControl), https://doi.org/10.22033/ESGF/CMIP6.4185 (CNRM-CM6-1-HR, ssp126), https://doi.org/10.22033/ESGF/CMIP6.4225 (CNRM-CM6-1-HR, ssp585) and https://doi.org/10.22033/ESGF/CMIP6.4066 (CNRM-CM6-1, historical). The CNRM-CM6-1-HR forcing fields are available on the ESGF website (https://esgf-

node.ipsl.upmc.fr/projects/esgf-ipsl/). The reanalyses data and altimetric observation product were obtained from the Copernicus Marine Services (https://marine.copernicus.eu/). MDT CNES CLS18 was produced by CLS and distributed by

805   Aviso +, with support from Cnes (https://www.aviso.altimetry.fr/). TG data records are obtained from the GESLA dataset (https://www.gesla.org/)

Supplement link

Author contribution:

AM designed the study. AV performed the global simulations. GR prepared the regional model configuration. AC prepared
810   the forcing files, performed the regional simulations and did the analyses. AM, AV and GR supervised the project. AC wrote the first draft of the manuscript. All author contributed to manuscript revision, read and approved the submitted version.

Competing interests:
All authors declare that they have no conflict of interest.

Disclaimer

815   **Acknowledgements**

Analyses were carried out with Python. The authors thank Romain Bourdallé-Badie for his useful technical advice on regional modeling.

Financial support

The PhD thesis of AC is supported by Mercator Ocean and Météo-France.
820

825

830

835

References

Adloff, F., Somot, S., Sevault, F., Jordà, G., Aznar, R., Déqué, M., Herrmann, M., Marcos, M., Dubois, C., Padorno, E., Alvarez-Fanjul, E., and Gomis, D.: Mediterranean Sea response to climate change in an ensemble of twenty first century
840   scenarios, Clim. Dyn., 45, 2775–2802, https://doi.org/10.1007/s00382-015-2507-3, 2015.

Adloff, F., Jordà, G., Somot, S., Sevault, F., Arsouze, T., Meyssignac, B., Li, L., and Planton, S.: Improving sea level simulation in Mediterranean regional climate models, Clim. Dyn., 51, 1167–1178, https://doi.org/10.1007/s00382-017-3842-3, 2018.

Barnier, B., Madec, G., Penduff, T., Molines, J.-M., Treguier, A.-M., Le Sommer, J., Beckmann, A., Biastoch, A., Böning,
845   C., Dengg, J., Derval, C., Durand, E., Gulev, S., Remy, E., Talandier, C., Theetten, S., Maltrud, M., McClean, J., and De Cuevas, B.: Impact of partial steps and momentum advection schemes in a global ocean circulation model at eddy-permitting resolution, Ocean Dyn., 56, 543–567, https://doi.org/10.1007/s10236-006-0082-1, 2006.

Berrisford, P., Dee, D., Fielding, K., Fuentes, M., Kallberg, P., Kobayashi, S., and Uppala, S.: The ERA-Interim Archive, ERA report series, European Centre for Medium-Range Weather Forecasts, Shinfield Park, Reading, 16 pp., 2009.

850   Blanke, B. and Delecluse, P.: Variability of the Tropical Atlantic Ocean Simulated by a General Circulation Model with Two Different Mixed-Layer Physics, J. Phys. Oceanogr., 23, 1363–1388, https://doi.org/10.1175/1520-0485(1993)023<1363:VOTTAO>2.0.CO;2, 1993.

Bozec, A., Lozier, M. S., Chassignet, E. P., and Halliwell, G. R.: On the variability of the Mediterranean Outflow Water in the North Atlantic from 1948 to 2006, J. Geophys. Res. Oceans, 116, https://doi.org/10.1029/2011JC007191, 2011.

855   Brodeau, L., Barnier, B., Gulev, S. K., and Woods, C.: Climatologically Significant Effects of Some Approximations in the Bulk Parameterizations of Turbulent Air–Sea Fluxes, J. Phys. Oceanogr., 47, 5–28, https://doi.org/10.1175/JPO-D-16-0169.1, 2017.

Chen, X., Zhou, T., Wu, P., Guo, Z., and Wang, M.: Emergent constraints on future projections of the western North Pacific Subtropical High, Nat. Commun., 11, 2802, https://doi.org/10.1038/s41467-020-16631-9, 2020.

860   Cordeiro, N. G. F., Dubert, J., Nolasco, R., and Barton, E. D.: Transient response of the Northwestern Iberian upwelling regime, PLOS ONE, 13, e0197627, https://doi.org/10.1371/journal.pone.0197627, 2018.

Dosio, A.: Projections of climate change indices of temperature and precipitation from an ensemble of bias-adjusted high-resolution EURO-CORDEX regional climate models, J. Geophys. Res. Atmospheres, 121, 5488–5511, https://doi.org/10.1002/2015JD024411, 2016.

865   Fasullo, J. T.: Evaluating simulated climate patterns from the CMIP archives using satellite and reanalysis datasets using the Climate Model Assessment Tool (CMATv1), Geosci. Model Dev., 13, 3627–3642, https://doi.org/10.5194/gmd-13-3627-2020, 2020.

Flather, R. A. and Davies, A. M.: Note on a preliminary scheme for storm surge prediction using numerical models, Q. J. R. Meteorol. Soc., 102, 123–132, https://doi.org/10.1002/qj.49710243110, 1976.

870   Fofonoff, N. P. and Millard Jr, R. C.: Algorithms for the computation of fundamental properties of seawater., https://doi.org/10.25607/OBP-1450, 1983.

Forget, G. and Ponte, R. M.: The partition of regional sea level variability, Prog. Oceanogr., 137, 173–195, https://doi.org/10.1016/j.pocean.2015.06.002, 2015.

Garric, G., Parent, L., Greiner, E., Drévillon, M., Hamon, M., Lellouche, J.-M., Régnier, C., Desportes, C., Le Galloudec, O.,
875   Bricaud, C., Drillet, Y., Hernandez, F., and Le Traon, P.-Y.: Performance and quality assessment of the global ocean eddy-permitting physical reanalysis GLORYS2V4., 18776, 2017.

Gaspar, P., Grégoris, Y., and Lefevre, J.-M.: A simple eddy kinetic energy model for simulations of the oceanic vertical mixing: Tests at station Papa and long-term upper ocean study site, J. Geophys. Res. Oceans, 95, 16179–16193, https://doi.org/10.1029/JC095iC09p16179, 1990.

880   Gomis, D., Álvarez-Fanjul, E., Jordà, G., Marcos, M., Aznar, R., Rodríguez-Camino, E., Sánchez-Perrino, J. C., Rodríguez-González, J. M., Martínez-Asensio, A., Llasses, J., Pérez, B., and Sotillo, M. G.: Regional marine climate scenarios in the NE Atlantic sector close to the Spanish shores, Sci. Mar., 80, 215–234, https://doi.org/10.3989/scimar.04328.07A, 2016.

Greatbatch, R. J.: A note on the representation of steric sea level in models that conserve volume rather than mass, J. Geophys. Res. Oceans, 99, 12767–12771, https://doi.org/10.1029/94JC00847, 1994.

885 Gregory, J. M., Griffies, S. M., Hughes, C. W., Lowe, J. A., Church, J. A., Fukimori, I., Gomez, N., Kopp, R. E., Landerer, F., Cozannet, G. L., Ponte, R. M., Stammer, D., Tamisiea, M. E., and van de Wal, R. S. W.: Concepts and Terminology for Sea Level: Mean, Variability and Change, Both Local and Global, Surv. Geophys., 40, 1251–1289, https://doi.org/10.1007/s10712-019-09525-z, 2019.

Griffies, S. M. and Greatbatch, R. J.: Physical processes that impact the evolution of global mean sea level in ocean climate
890 models, Ocean Model., 51, 37–72, https://doi.org/10.1016/j.ocemod.2012.04.003, 2012.

Grinsted, A. and Christensen, J. H.: The transient sensitivity of sea level rise, Ocean Sci., 17, 181–186, https://doi.org/10.5194/os-17-181-2021, 2021.

Grinsted, A., Jevrejeva, S., Riva, R. E. M., and Dahl-Jensen, D.: Sea level rise projections for northern Europe under RCP8.5, Clim. Res., 64, 15–23, https://doi.org/10.3354/cr01309, 2015.

895 Gupta, A. S., Jourdain, N. C., Brown, J. N., and Monselesan, D.: Climate Drift in the CMIP5 Models, J. Clim., 26, 8597–8615, https://doi.org/10.1175/JCLI-D-12-00521.1, 2013.

Hallberg, R.: Using a resolution function to regulate parameterizations of oceanic mesoscale eddy effects, Ocean Model., 72, 92–103, https://doi.org/10.1016/j.ocemod.2013.08.007, 2013.

Hermans, T. H. J., Tinker, J., Palmer, M. D., Katsman, C. A., Vermeersen, B. L. A., and Slangen, A. B. A.: Improving sea-
900 level projections on the Northwestern European shelf using dynamical downscaling, Clim. Dyn., 54, 1987–2011, https://doi.org/10.1007/s00382-019-05104-5, 2020.

Hernández-Díaz, L., Nikiéma, O., Laprise, R., Winger, K., and Dandoy, S.: Effect of empirical correction of sea-surface temperature biases on the CRCM5-simulated climate and projected climate changes over North America, Clim. Dyn., 53, 453–476, https://doi.org/10.1007/s00382-018-4596-2, 2019.

905 Hock, R., Bliss, A., Marzeion, B., Giesen, R. H., Hirabayashi, Y., Huss, M., Radić, V., and Slangen, A. B. A.: GlacierMIP – A model intercomparison of global-scale glacier mass-balance models and projections, J. Glaciol., 65, 453–467, https://doi.org/10.1017/jog.2019.22, 2019.

Idier, D., Paris, F., Cozannet, G. L., Boulahya, F., and Dumas, F.: Sea-level rise impacts on the tides of the European Shelf, Cont. Shelf Res., 137, 56–71, https://doi.org/10.1016/j.csr.2017.01.007, 2017.

910 Irving, D., Hobbs, W., Church, J., and Zika, J.: A Mass and Energy Conservation Analysis of Drift in the CMIP6 Ensemble, J. Clim., 34, 3157–3170, https://doi.org/10.1175/JCLI-D-20-0281.1, 2021.

Jin, Y., Zhang, X., Church, J. A., and Bao, X.: Projected Sea Level Changes in the Marginal Seas near China Based on Dynamical Downscaling, J. Clim., 34, 7037–7055, https://doi.org/10.1175/JCLI-D-20-0796.1, 2021.

Kopp, R. E., Horton, R. M., Little, C. M., Mitrovica, J. X., Oppenheimer, M., Rasmussen, D. J., Strauss, B. H., and Tebaldi,
915 C.: Probabilistic 21st and 22nd century sea-level projections at a global network of tide-gauge sites, Earths Future, 2, 383–406, https://doi.org/10.1002/2014EF000239, 2014.

Krinner, G. and Flanner, M. G.: Striking stationarity of large-scale climate model bias patterns under strong climate change, Proc. Natl. Acad. Sci. U. S. A., 115, 9462–9466, https://doi.org/10.1073/pnas.1807912115, 2018.

Lavergne, C. de, Vic, C., Madec, G., Roquet, F., Waterhouse, A. F., Whalen, C. B., Cuypers, Y., Bouruet-Aubertot, P.,
920 Ferron, B., and Hibiya, T.: A Parameterization of Local and Remote Tidal Mixing, J. Adv. Model. Earth Syst., 12, e2020MS002065, https://doi.org/10.1029/2020MS002065, 2020.

Leonard, B. P.: A stable and accurate convective modelling procedure based on quadratic upstream interpolation, Comput. Methods Appl. Mech. Eng., 19, 59–98, https://doi.org/10.1016/0045-7825(79)90034-3, 1979.

Liu, Z.-J., Minobe, S., Sasaki, Y. N., and Terada, M.: Dynamical downscaling of future sea level change in the western
925 North Pacific using ROMS, J. Oceanogr., 72, 905–922, https://doi.org/10.1007/s10872-016-0390-0, 2016.

Macias, D., Garcia-Gorriz, E., Dosio, A., Stips, A., and Keuler, K.: Obtaining the correct sea surface temperature: bias correction of regional climate model data for the Mediterranean Sea, Clim. Dyn., 51, 1095–1117, https://doi.org/10.1007/s00382-016-3049-z, 2018.

930 Madec, G., Bourdallé-Badie, R., Bouttier, P.-A., Bricaud, C., Bruciaferri, D., Calvert, D., Chanut, J., Clementi, E., Coward, A., Delrosso, D., Ethé, C., Flavoni, S., Graham, T., Harle, J., Iovino, D., Lea, D., Lévy, C., Lovato, T., Martin, N., Masson, S., Mocavero, S., Paul, J., Rousset, C., Storkey, D., Storto, A., and Vancoppenolle, M.: NEMO ocean engine, https://doi.org/10.5281/zenodo.3248739, 2017.

Maraldi, C., Chanut, J., Levier, B., Ayoub, N., De Mey, P., Reffray, G., Lyard, F., Cailleau, S., Drévillon, M., Fanjul, E. A., Sotillo, M. G., and Marsaleix, P.: NEMO on the shelf: assessment of the Iberia-Biscay-Ireland configuration, All 935 Depths/Operational Oceanography/All Geographic Regions/Temperature, Salinity and Density Fields, https://doi.org/10.5194/osd-10-83-2013, 2013.

Mathis, M., Mayer, B., and Pohlmann, T.: An uncoupled dynamical downscaling for the North Sea: Method and evaluation, Ocean Model., 72, 153–166, https://doi.org/10.1016/j.ocemod.2013.09.004, 2013.

McGranahan, G., Balk, D., and Anderson, B.: The rising tide: assessing the risks of climate change and human settlements in 940 low elevation coastal zones, Environ. Urban., 19, 17–37, https://doi.org/10.1177/0956247807076960, 2007.

Melet, A., Meyssignac, B., Almar, R., and Le Cozannet, G.: Under-estimated wave contribution to coastal sea-level rise, Nat. Clim. Change, 8, 234–239, https://doi.org/10.1038/s41558-018-0088-y, 2018.

Melet, A., Almar, R., Hemer, M., Cozannet, G. L., Meyssignac, B., and Ruggiero, P.: Contribution of Wave Setup to Projected Coastal Sea Level Changes, J. Geophys. Res. Oceans, 125, e2020JC016078, 945 https://doi.org/10.1029/2020JC016078, 2020.

Menéndez, M. and Woodworth, P. L.: Changes in extreme high water levels based on a quasi-global tide-gauge data set, J. Geophys. Res. Oceans, 115, https://doi.org/10.1029/2009JC005997, 2010.

Meyssignac, B., Piecuch, C. G., Merchant, C. J., Racault, M.-F., Palanisamy, H., MacIntosh, C., Sathyendranath, S., and Brewin, R.: Causes of the Regional Variability in Observed Sea Level, Sea Surface Temperature and Ocean Colour Over the 950 Period 1993–2011, Surv. Geophys., 38, 187–215, https://doi.org/10.1007/s10712-016-9383-1, 2017a.

Meyssignac, B., Slangen, A. B. A., Melet, A., Church, J. A., Fettweis, X., Marzeion, B., Agosta, C., Ligtenberg, S. R. M., Spada, G., Richter, K., Palmer, M. D., Roberts, C. D., and Champollion, N.: Evaluating Model Simulations of Twentieth-Century Sea-Level Rise. Part II: Regional Sea-Level Changes, J. Clim., 30, 8565–8593, https://doi.org/10.1175/JCLI-D-17-0112.1, 2017b.

955 Muis, S., Apecechea, M. I., Dullaart, J., de Lima Rego, J., Madsen, K. S., Su, J., Yan, K., and Verlaan, M.: A High-Resolution Global Dataset of Extreme Sea Levels, Tides, and Storm Surges, Including Future Projections, Front. Mar. Sci., 7, 263, https://doi.org/10.3389/fmars.2020.00263, 2020.

Mulet, S., Rio, M.-H., Etienne, H., Artana, C., Cancet, M., Dibarboure, G., Feng, H., Husson, R., Picot, N., Provost, C., and Strub, P. T.: The new CNES-CLS18 global mean dynamic topography, Ocean Sci., 17, 789–808, https://doi.org/10.5194/os-960 17-789-2021, 2021.

Neumann, B., Vafeidis, A. T., Zimmermann, J., and Nicholls, R. J.: Future Coastal Population Growth and Exposure to Sea-Level Rise and Coastal Flooding - A Global Assessment, PLOS ONE, 10, e0118571, https://doi.org/10.1371/journal.pone.0118571, 2015.

O'Neill, B. C., Tebaldi, C., van Vuuren, D. P., Eyring, V., Friedlingstein, P., Hurtt, G., Knutti, R., Kriegler, E., Lamarque, J.-965 F., Lowe, J., Meehl, G. A., Moss, R., Riahi, K., and Sanderson, B. M.: The Scenario Model Intercomparison Project (ScenarioMIP) for CMIP6, Geosci. Model Dev., 9, 3461–3482, https://doi.org/10.5194/gmd-9-3461-2016, 2016.

Reffray, G., Bourdalle-Badie, R., and Calone, C.: Modelling turbulent vertical mixing sensitivity using a 1-D version of NEMO, Geosci. Model Dev., 8, 69–86, https://doi.org/10.5194/gmd-8-69-2015, 2015.

Richter, K., Riva, R. E. M., and Drange, H.: Impact of self-attraction and loading effects induced by shelf mass loading on 970 projected regional sea level rise, Geophys. Res. Lett., 40, 1144–1148, https://doi.org/10.1002/grl.50265, 2013.

Roehrig, R., Beau, I., Saint-Martin, D., Alias, A., Decharme, B., Guérémy, J.-F., Voldoire, A., Abdel-Lathif, A. Y., Bazile, E., Belamari, S., Blein, S., Bouniol, D., Bouteloup, Y., Cattiaux, J., Chauvin, F., Chevallier, M., Colin, J., Douville, H.,

Marquet, P., Michou, M., Nabat, P., Oudar, T., Peyrillé, P., Piriou, J.-M., Salas y Mélia, D., Séférian, R., and Sénési, S.: The CNRM Global Atmosphere Model ARPEGE-Climat 6.3: Description and Evaluation, J. Adv. Model. Earth Syst., 12, e2020MS002075, https://doi.org/10.1029/2020MS002075, 2020.

Roquet, F., Madec, G., Brodeau, L., and Nycander, J.: Defining a Simplified Yet "Realistic" Equation of State for Seawater, J. Phys. Oceanogr., 45, 2564–2579, https://doi.org/10.1175/JPO-D-15-0080.1, 2015.

Shin, S.-I. and Alexander, M. A.: Dynamical Downscaling of Future Hydrographic Changes over the Northwest Atlantic Ocean, J. Clim., 33, 2871–2890, https://doi.org/10.1175/JCLI-D-19-0483.1, 2020.

Slangen, A. B. A., Carson, M., Katsman, C. A., van de Wal, R. S. W., Köhl, A., Vermeersen, L. L. A., and Stammer, D.: Projecting twenty-first century regional sea-level changes, Clim. Change, 124, 317–332, https://doi.org/10.1007/s10584-014-1080-9, 2014.

Slangen, A. B. A., Meyssignac, B., Agosta, C., Champollion, N., Church, J. A., Fettweis, X., Ligtenberg, S. R. M., Marzeion, B., Melet, A., Palmer, M. D., Richter, K., Roberts, C. D., and Spada, G.: Evaluating Model Simulations of Twentieth-Century Sea Level Rise. Part I: Global Mean Sea Level Change, J. Clim., 30, 8539–8563, https://doi.org/10.1175/JCLI-D-17-0110.1, 2017.

Sotillo, M. G., Cailleau, S., Lorente, P., Levier, B., Aznar, R., Reffray, G., Amo-Baladrón, A., Chanut, J., Benkiran, M., and Alvarez-Fanjul, E.: The MyOcean IBI Ocean Forecast and Reanalysis Systems: operational products and roadmap to the future Copernicus Service, J. Oper. Oceanogr., 8, 63–79, https://doi.org/10.1080/1755876X.2015.1014663, 2015.

Soto-Navarro, J., Criado-Aldeanueva, F., García-Lafuente, J., and Sánchez-Román, A.: Estimation of the Atlantic inflow through the Strait of Gibraltar from climatological and in situ data, J. Geophys. Res. Oceans, 115, https://doi.org/10.1029/2010JC006302, 2010.

Soto-Navarro, J., Somot, S., Sevault, F., Beuvier, J., Criado-Aldeanueva, F., García-Lafuente, J., and Béranger, K.: Evaluation of regional ocean circulation models for the Mediterranean Sea at the Strait of Gibraltar: volume transport and thermohaline properties of the outflow, Clim. Dyn., 44, 1277–1292, https://doi.org/10.1007/s00382-014-2179-4, 2015.

Soto-Navarro, J., Jordá, G., Amores, A., Cabos, W., Somot, S., Sevault, F., Macías, D., Djurdjevic, V., Sannino, G., Li, L., and Sein, D.: Evolution of Mediterranean Sea water properties under climate change scenarios in the Med-CORDEX ensemble, Clim. Dyn., 54, 2135–2165, https://doi.org/10.1007/s00382-019-05105-4, 2020.

Stammer, D. and Hüttemann, S.: Response of Regional Sea Level to Atmospheric Pressure Loading in a Climate Change Scenario, J. Clim., 21, 2093–2101, https://doi.org/10.1175/2007JCLI1803.1, 2008.

Takayabu, I., Kanamaru, H., Dairaku, K., Benestad, R., Storch, H. von, and Christensen, J. H.: Reconsidering the Quality and Utility of Downscaling, J. Meteorol. Soc. Jpn. Ser II, 94A, 31–45, https://doi.org/10.2151/jmsj.2015-042, 2016.

Umlauf, L. and Burchard, H.: A generic length-scale equation for geophysical turbulence models, J. Mar. Res., 61, 235–265, https://doi.org/10.1357/002224003322005087, 2003.

Voldoire, A.: River to ocean models interpolation, report, CNRM, Université de Toulouse, Météo-France, CNRS, 2020.

Voldoire, A., Saint-Martin, D., Sénési, S., Decharme, B., Alias, A., Chevallier, M., Colin, J., Guérémy, J.-F., Michou, M., Moine, M.-P., Nabat, P., Roehrig, R., Mélia, D. S. y, Séférian, R., Valcke, S., Beau, I., Belamari, S., Berthet, S., Cassou, C., Cattiaux, J., Deshayes, J., Douville, H., Ethé, C., Franchistéguy, L., Geoffroy, O., Lévy, C., Madec, G., Meurdesoif, Y., Msadek, R., Ribes, A., Sanchez-Gomez, E., Terray, L., and Waldman, R.: Evaluation of CMIP6 DECK Experiments With CNRM-CM6-1, J. Adv. Model. Earth Syst., 11, 2177–2213, https://doi.org/10.1029/2019MS001683, 2019.

Vousdoukas, M. I., Mentaschi, L., Voukouvalas, E., Bianchi, A., Dottori, F., and Feyen, L.: Climatic and socioeconomic controls of future coastal flood risk in Europe, Nat. Clim. Change, 8, 776–780, https://doi.org/10.1038/s41558-018-0260-4, 2018a.

Vousdoukas, M. I., Mentaschi, L., Voukouvalas, E., Verlaan, M., Jevrejeva, S., Jackson, L. P., and Feyen, L.: Global probabilistic projections of extreme sea levels show intensification of coastal flood hazard, Nat. Commun., 9, 2360, https://doi.org/10.1038/s41467-018-04692-w, 2018b.

van Westen, R. M., Dijkstra, H. A., van der Boog, C. G., Katsman, C. A., James, R. K., Bouma, T. J., Kleptsova, O., Klees, R., Riva, R. E. M., Slobbe, D. C., Zijlema, M., and Pietrzak, J. D.: Ocean model resolution dependence of Caribbean sea-level projections, Sci. Rep., 10, 14599, https://doi.org/10.1038/s41598-020-71563-0, 2020.

1020   Woodworth, P. L., Hunter, J. R., Marcos, M., Caldwell, P., Menéndez, M., and Haigh, I.: Towards a global higher-frequency sea level dataset, Geosci. Data J., 3, 50–59, https://doi.org/10.1002/gdj3.42, 2017.

Woodworth, P. L., Melet, A., Marcos, M., Ray, R. D., Wöppelmann, G., Sasaki, Y. N., Cirano, M., Hibbert, A., Huthnance, J. M., Monserrat, S., and Merrifield, M. A.: Forcing Factors Affecting Sea Level Changes at the Coast, Surv. Geophys., 40, 1351–1397, https://doi.org/10.1007/s10712-019-09531-1, 2019.

1025   Xu, Z., Han, Y., and Yang, Z.: Dynamical downscaling of regional climate: A review of methods and limitations, Sci. China Earth Sci., 62, 365–375, https://doi.org/10.1007/s11430-018-9261-5, 2019.

Zalesak, S. T.: Fully multidimensional flux-corrected transport algorithms for fluids, J. Comput. Phys., 31, 335–362, https://doi.org/10.1016/0021-9991(79)90051-2, 1979.

Zhang, X., Church, J. A., Monselesan, D., and McInnes, K. L.: Sea level projections for the Australian region in the 21st
1030   century, Geophys. Res. Lett., 44, 8481–8491, https://doi.org/10.1002/2017GL074176, 2017.